

LIQUID LITHIUM CORROSION OF
NITRIDED 304L STAINLESS STEEL

by

John Allen Reeves

ProQuest Number: 10781941

All rights reserved

INFORMATION TO ALL USERS

The quality of this reproduction is dependent upon the quality of the copy submitted.

In the unlikely event that the author did not send a complete manuscript and there are missing pages, these will be noted. Also, if material had to be removed, a note will indicate the deletion.



ProQuest 10781941

Published by ProQuest LLC (2018). Copyright of the Dissertation is held by the Author.

All rights reserved.

This work is protected against unauthorized copying under Title 17, United States Code
Microform Edition © ProQuest LLC.

ProQuest LLC.
789 East Eisenhower Parkway
P.O. Box 1346
Ann Arbor, MI 48106 – 1346

SUBMITTAL SHEET

A Thesis submitted to the Faculty and the Board of Trustees of the Colorado School of Mines in partial fulfillment of the requirements for the degree of Masters of Science, Metallurgical Engineering.

Signed: John A. Reavis
Student

Golden, Colorado

Date: 10/14, 1974

Approved: David L. Olson
Thesis Advisor

[Signature]
Head of Department

Golden, Colorado

Date: 10/15, 1974

ARTS
COLORADO
GOLDEN, COLORADO 80401

ABSTRACT

Grain boundary penetration and weight loss were determined for a nitrided 304L stainless steel in a nitrogen saturated lithium system. These results, along with previous work with as-received 304L stainless steel were used to develop a theoretical corrosion model.

The thermally activated grain boundary penetration obeyed a parabolic rate law. However, nitriding, increasing the penetration rate, did not cause a mechanistic change. A delay time, observed before the penetration started, was needed to incubate a (Li-Me-N) corrosion complex. The penetration was controlled by the diffusion of lithium through the incubated complex, located in the penetrated grain boundaries. The activation energies, for the nitrided and as-received specimens, indicated the (Li-Me-N) complex exhibited a solid-liquid transition at 747° C.

The parabolic weight loss had a duplex behavior. The duplex initiated with a thermally activated uniform corrosion followed by an irregular surface deterioration. The activation energies for the initial process were consistent with the above liquid-solid transition.

In general, increasing the nitrogen content of the 304L stainless steel increased penetration and weight loss. However, this increase did not result in a mechanistic change.

TABLE OF CONTENTS

	<u>Page</u>
INTRODUCTION	1
Properties of Liquid Lithium	1
Principal Types of Corrosion	10
Simple Solution	10
Alloying	14
Intergranular Penetration	18
Impurity Effects	23
Temperature Gradient Mass Transfer	27
Dissimilar Metal Effects	28
Theoretical Presentation by Brehm	30
Theoretical Presentation by Patterson	34
Uniform Corrosion Theory	39
OBJECTIVES	40
EXPERIMENTAL PROCEDURE	41
Materials	41
Apparatus	41
Testing	45
DISCUSSION AND RESULTS	52
Grain-Boundary Penetration	52

	<u>Page</u>
DISCUSSION AND RESULTS (continued)	
Uniform Corrosion and Weight Loss	67
CONCLUSIONS	78
SUGGESTIONS FOR FURTHER RESEARCH	79
APPENDIX I	80
REFERENCES	83

LIST OF FIGURES

<u>Figure</u>		<u>Page</u>
1.	Resistance of materials to attack by lithium. ⁽⁴⁷⁾	7
2.	Resistance of materials to lithium corrosion. ⁽⁴⁷⁾	8
3.	Corrosion resistance of various metals and alloys in static and dynamic lithium. ⁽⁴⁰⁾	9
4.	The temperature dependence of the solubilities of a number of metals. ⁽⁵²⁾	11
5.	The solubility of niobium and titanium as a function of temperature and nitrogen concentration of liquid lithium. ⁽⁵²⁾	13
6.	Comparison of the corrosion rates of stainless steel as a function of temperature and oxygen concentration of liquid sodium. ⁽³⁷⁾	15
7.	The lithium-aluminum equilibrium phase diagram determined by Lithium Corporation of America. ⁽⁶⁵⁾	16
8.	Temperature dependence of sodium and potassium diffusing into (1) Armco iron and (2) electrolytic iron. ⁽³⁶⁾	17
9.	Arrhenius plot for grain boundary penetration into oxygen doped niobium by liquid lithium. ⁽⁴⁸⁾	20
10.	The time needed to nucleate a metal carbide in 316-L stainless steel compared with the delay time in a 304-L stainless steel-lithium system. ^(71, 74)	24

<u>Figure</u>	<u>Page</u>
11. The Li_3N portion of the lithium-nitrogen equilibrium phase diagram. (65)	25
12. A schematic diagram of the concept of a loop containing flowing liquid metal in the presence of temperature gradients. (40)	28
13. A schematic diagram showing the mass transport possible in the presence of dissimilar metals or concentration gradients. (71)	29
14. Penetrated zone and concentration profile as assumed by Brehm. (48,49)	31
15. Penetration zone, chemical potential profile, and concentration profile as assumed by Patterson. (71)	35
16. Nitrogen diffusion in an 18% chromium, 12% nickel, iron alloy. (82)	42
17. Grain growth curve at 1100°C for annealing 304-L stainless steel in an ammonia atmosphere.	43
18. A photo-micrograph showing the as annealed nitrided microstructure.	44
19. A schematic diagram of the test crucible and sample arrangement used in this investigation.	46
20. Photo-micrograph showing the penetration pattern as revealed by the two etches.	51

<u>Figure</u>	<u>Page</u>
21. Bend test showing sample cracking after exposure to liquid lithium at 800 ^o C, 9 hours.	53
22. A graph of penetration depth versus the square root of time at 800 ^o C for as-received 304-L stainless steel. ⁽⁷¹⁾	54
23. A graph of penetration depth versus the square root of time at 600 ^o C for as-received ⁽⁷¹⁾ and nitrided 304-L stainless steel.	55
24. A graph of penetration depth versus the square root of time at 650 ^o C for as-received ⁽⁷¹⁾ and nitrided 304-L stainless steel.	56
25. A graph of penetration depth versus the square root of time at 700 ^o C for nitrided 304-L stainless steel.	57
26. A graph of penetration depth versus the square root of time at 750 ^o C for nitrided 304-L stainless steel.	58
27. A graph of penetration depth versus the square root of time at 800 ^o C for as-received ⁽⁷¹⁾ and nitrided 304-L stainless steel.	59
28. A graph of penetration depth versus the square root of time at 900 ^o C for as-received ⁽⁷¹⁾ and nitrided 304-L stainless steel.	60

<u>Figure</u>	<u>Page</u>
29. An Arrhenius plot showing the temperature dependence of grain-boundary penetration rate for as-received ⁽⁷¹⁾ and nitrided 304-L stainless steel.	62
30. The time needed to nucleate a metal carbide in 316-L stainless steel ⁽⁷⁴⁾ compared with the delay times in as-received ⁽⁷¹⁾ and nitrided 304-L stainless steel.	66
31. A graph of weight loss per unit surface area versus the square root of time at 600 ⁰ C for as-received ⁽⁷¹⁾ and nitrided 304-L stainless steel.	68
32. A graph of weight loss per unit surface area versus the square root of time at 650 ⁰ C for as-received ⁽⁷¹⁾ and nitrided 304-L stainless steel.	69
33. A graph of weight loss per unit surface area versus the square root of time at 700 ⁰ C for nitrided 304-L stainless steel.	70
34. A graph of weight loss per unit surface area versus the square root of time at 750 ⁰ C for nitrided 304-L stainless steel.	71
35. A graph of weight loss per unit surface area versus the square root of time at 900 ⁰ C for as-received ⁽⁷¹⁾ and nitrided 304-L stainless steel.	72

<u>Figure</u>		<u>Page</u>
36.	A photo-micrograph showing transgranular penetration of nitrided 304-L stainless steel by liquid lithium at 800 ^o C, for 25 hours.	73
37.	A photo-micrograph showing surface deterioration and degradation of nitrided 304-L stainless steel by liquid lithium at 800 ^o C for 144 hours.	75
38.	A graph showing the temperature dependence for the initial slope of the nitrided 304-L stainless steel weight loss curves.	76

LIST OF TABLES

<u>Table</u>	<u>Page</u>
I. Physical properties of metals and water.(39,41,42)	2
II. Physical properties of metals and water.(39,41,42)	4
III. Neutron-absorption cross sections.(43-45)	5
IV. Li_3N effects on the corrosion of type 316 ⁽⁴⁰⁾ stainless steel in liquid lithium.	22
V. Matrix of test performed.	47
VI. Chemical etches and procedures used for metallography.	49
VII. Grain boundary penetration rate coefficients.	65
VIII. Activation energies for grain boundary penetration.	65
IX. Weight loss rate coefficients and activation energy.	77

ACKNOWLEDGEMENTS

The author gratefully appreciates the expert guidance and advice provided by his thesis advisor, Dr. D. L. Olson, and the thesis committee, Dr. W. L. Bradley and Dr. D. K. Matlock.

Financial support for this investigation was provided by the Atomic Energy Commission.

INTRODUCTION

With the advent of today's high-temperature nuclear technology, the development of an efficient heat-transfer medium is important. The fast breeder reactors and the proposed fusion power plants of the future will produce large quantities of heat which the traditional coolants, water and gas, will be incapable of handling. Other coolants, including liquid sodium-potassium alloys⁽¹⁻³⁸⁾ and lithium⁽³⁹⁾, have been investigated and found superior.

The desired properties⁽⁴⁰⁾ for a high-temperature nuclear-reactor coolant are:

- (1) Low neutron cross-section (for thermal reactors)
- (2) Low melting point
- (3) High boiling point
- (4) Low vapor pressure at high temperatures
- (5) Low density
- (6) High heat capacity
- (7) High thermal conductivity
- (8) Low viscosity

The principal properties^(39, 41, 42) of the possible reactor coolants are presented in table I. Lithium has a high boiling point and a low melting point. Lithium has the largest liquid temperature range of any of the alkali metals. At high

TABLE I. PHYSICAL PROPERTIES OF METALS AND WATER (39, 41, 42)

	Melting Point (C)	Boiling Point (C)	Temp. for 10 mm Hg Vapor Pressure (C)	Density (gm/cm ³)	Capacity (cal/gm C)	Latent Heat of Vaporization (cal/mole)
Lithium	179	1317	890	(800 C) 0.46	1.0	4680
Sodium	98	883	548	(700 C) 0.78	0.31	1005
Sodium-Potassium	-11	784	458	(700 C) 0.70	0.21	-
44% Potassium Lead	327	1737	1167	(800 C) 10.04	0.037	205
Mercury	-39	357	184	(300 C) 12.88	0.032	70
Water	0	100	11	(4 C) 1.0	1.0	540
Bismuth	271	1477	1067	(800 C) 9.40	0.04	204
Lead-Bismuth	125	1670	1100	(800 C) 9.64	0.035	-

temperatures lithium can be used at near-atmospheric pressure. Since it can maintain a low vapor pressure, the structural integrity of the coolant system is not a limiting factor. Lithium is the lightest solid element and has a heat capacity equaled only by water. Also, lithium has an extremely high heat of vaporization.

In table II, (39,41,42) it can be seen that thermal conductivity of lithium is surpassed only by sodium, while it has more than twice the heat of fusion of any other material. The viscosity of lithium is moderate but its volume change upon fusion and electrical resistance are low. The electrical resistance of a medium is important when electromagnetic pumping is considered.

The neutron absorption cross-sections of the coolants are shown in table III. (43-45) Natural-occurring lithium, 92.5% lithium-7, 7.5% lithium-6, has a weighted neutron cross-section of 70 barns. A high neutron cross-section⁽⁴⁵⁾ is detrimental to efficient thermal reactor operation. However, lithium-7 and lithium-6 can be isotopically separated. Recent developments indicate separation is not a serious problem. (40,46) Another advantage of lithium-7 is (39,41,46) that upon neutron capture it becomes lithium-8 which has a half life of .85 seconds. Thus in a circulating loop, very little radiation would be transferred outside the primary reactor shielding to a heat exchanger. This is a major consideration when inspection and

TABLE II. PHYSICAL PROPERTIES OF METALS AND WATER (39, 41, 42)

	Thermal Conductivity (cal/sec-cm C)	Latent Heat of Fusion (cal/gm)	Viscosity (centipoises)	Volume Change on Fusion (% of Solid Volume)	Electrical Resistivity (ohms)
Lithium	0.09	158	(980 C) 0.41	1.5	(230 C) 45.3
Sodium	0.16	27	(700 C) 0.41	2.5	(300 C) 16.7
Sodium-Potassium 44% Potassium	0.06	-	(700 C) 0.15	2.5	(200 C) 47.0
Lead	0.036	5.8	(845 C) 1.19	3.6	(327 C) 94.6
Mercury	0.03	2.8	(200 C) 1.0	3.6	(300 C) 127.5
Water	0.001	79.0	(100 C) 0.28	-8.3	-
Bismuth	0.037	12.0	(600 C) 1.0	-3.3	(300 C) 128.9
Lead-Bismuth 55.5% Bismuth	0.026	-	(600 C) 1.17	0.0	(300 C) 118.0

TABLE III. NEUTRON-ABSORPTION CROSS SECTIONS (43-45)

	<u>Macroscopic at 343 C cm⁻¹</u>	<u>Barns cm² X 10⁻²⁴</u>
Sodium-23	0.0074	0.45
Potassium	0.0166	2.5
Lithium-6		984.0
Lithium-7	0.00097	0.033
Bismuth-209	0.00059	0.03
Sodium-Potassium 44% Potassium	0.0113	1.1
Lead-Magnesium 2.5% Magnesium	0.0040	0.21
Bismuth-Lead 44.5% Lead	0.0021	0.17

repair of the system are performed.

High-temperature liquid lithium, with all its favorable properties, is extremely corrosive. There are no known common construction materials which will contain high-temperature liquid lithium for an indefinite period of time.

The initial effort in choosing a container for liquid lithium was to qualitatively screen available materials. The preliminary static tests, shown in figures 1 and 2⁽⁴⁷⁾ indicate that pure iron followed by beryllium and stainless steels have good resistance. Similar tests show the refractory alloys, niobium, tantalum, and zirconium have also excellent resistance to lithium.^(14,48-50) However, in a dynamic system the static corrosive integrity is destroyed. To date, as shown in figure 3, the only known metals^(40,51) which seem appropriate for application in dynamic, non-isothermal systems operating in excess of 650° C. are refractory alloys.

Many tests have been performed to determine the best container material for a given set of alkali-metal conditions. The ultimate goal of any test is to simulate the environment the containment metal will experience. Corrosion tests are usually classified as either static or dynamic. In general, the various tests are:⁽¹⁴⁾

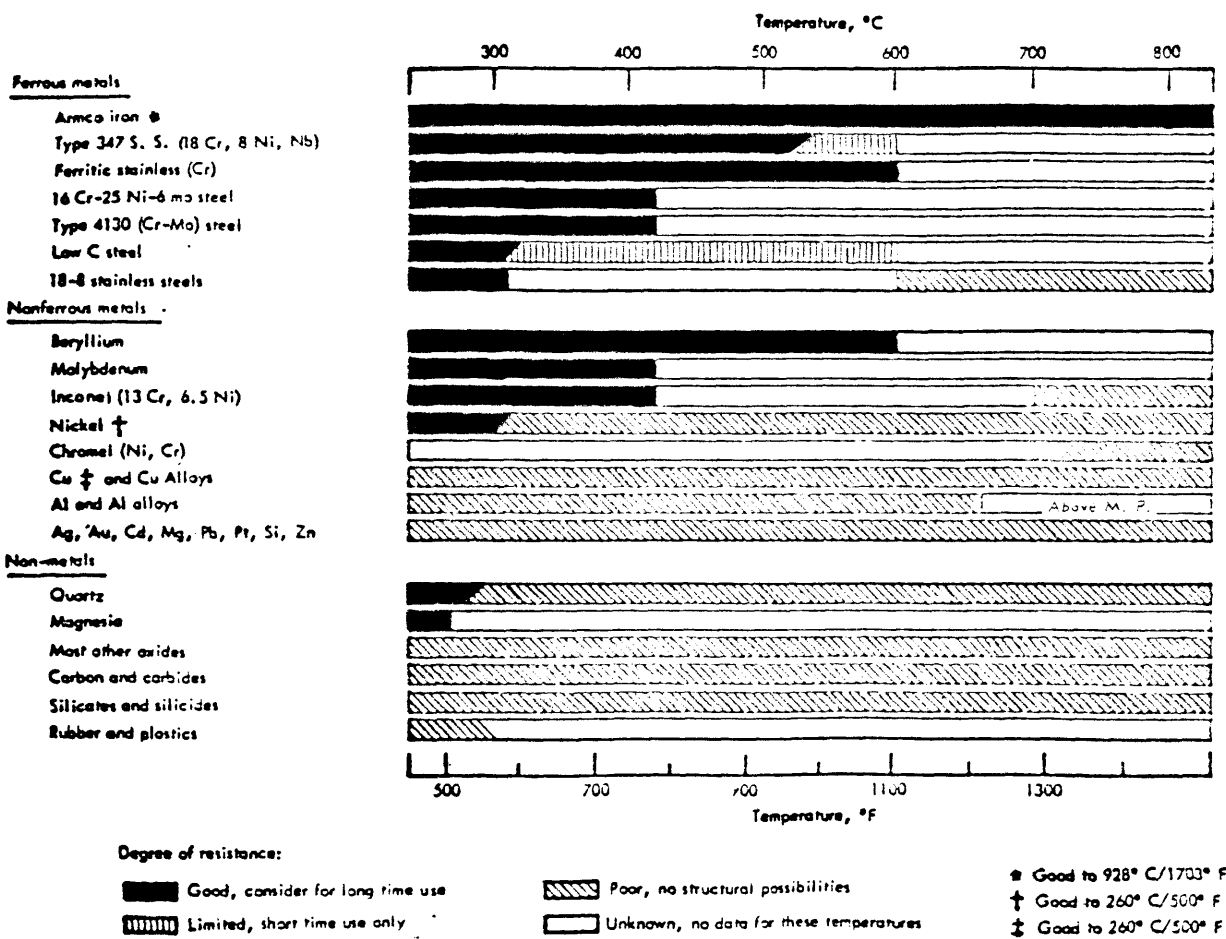


Figure 1. Resistance of materials to attack by lithium. (47)

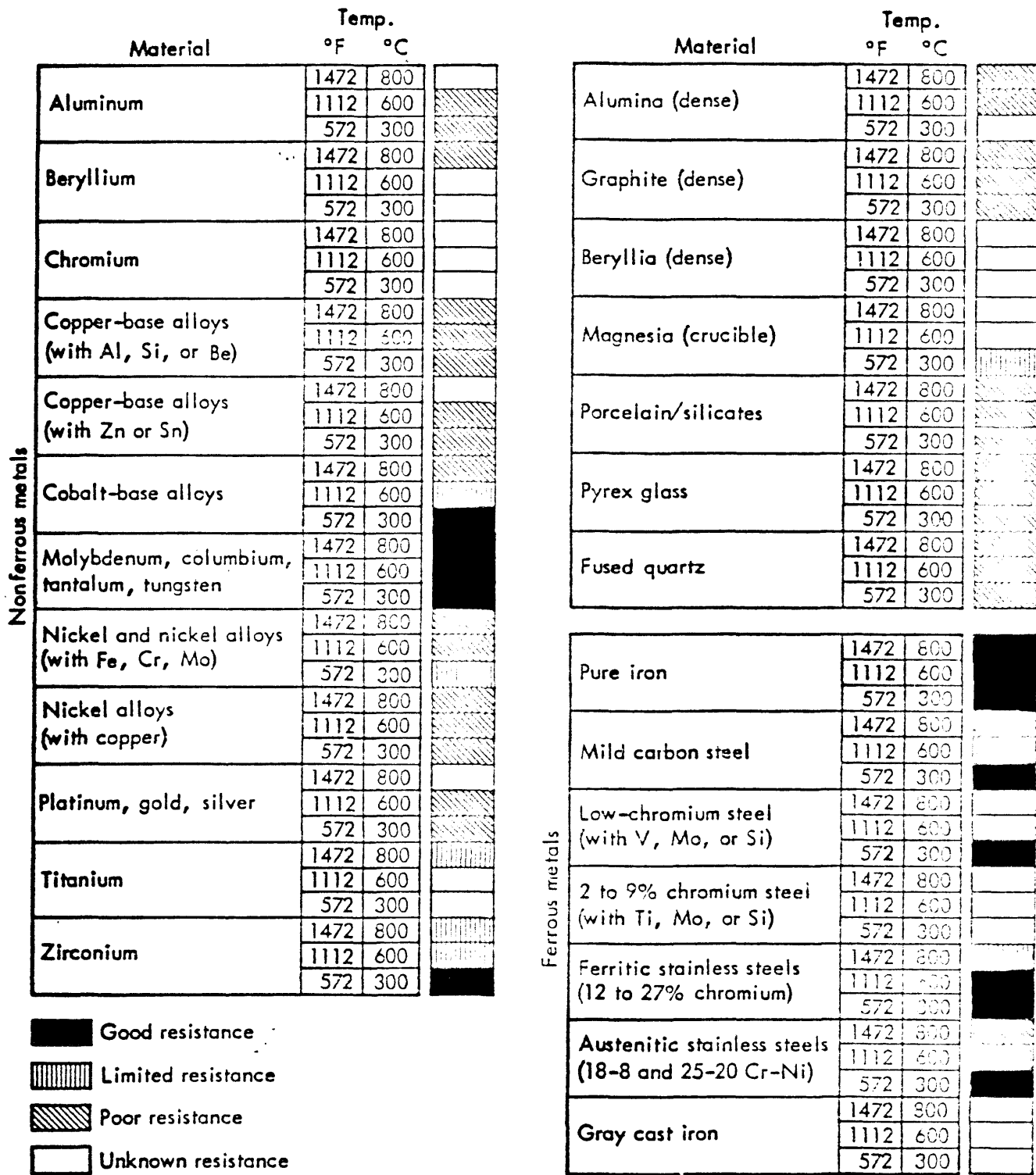


Figure 2. Resistance of materials to lithium corrosion. (47)

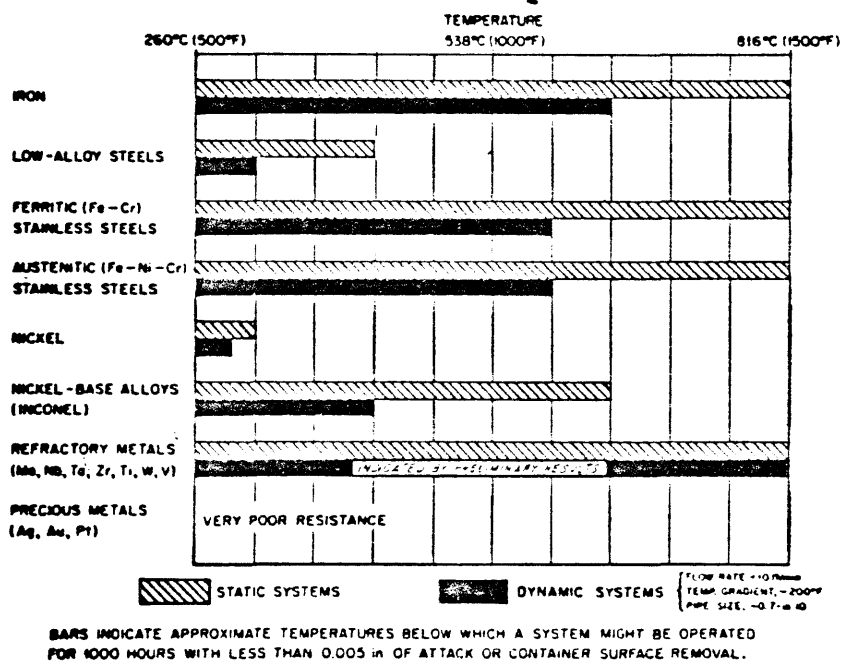


Figure 3. Corrosion resistance of various metals and alloys in static and dynamic lithium. (40)

Static Tests

- (1) No movement of liquid; no temperature gradients

Dynamic Tests

- (1) Low velocity (2 to 10 feet per minute)
- (2) Seesaw or tilting tests. A sealed tube partially filled with liquid metal is tilted up and down.
- (3) Thermal-convection loops. A sealed loop filled with a liquid metal is heated in certain sections and cooled in others to cause circulation due to changes in density of the liquid metal.
- (4) Dynamic tests, high velocity (2 to 50 feet per second) flow induced by electromagnetic or mechanical pumps.

Static tests are easy to perform and interpret, while dynamic tests involve a multiplicity of interactions. In the most general corrosion system, a high-velocity dynamic test, the principal types of liquid metal corrosion are:⁽⁴⁰⁾

Simple Solution: Simple solution is the attempt of the system to achieve solubility equilibrium between the containment metal and alkali metal. This phenomenon has been investigated by many researchers to date.^(37,52-56) A measure of simple solution or dissolution is weight loss. Shown in figure 4 are the solubilities of nickel, chromium, iron, titanium and molybdenum in lithium. The solubility of niobium

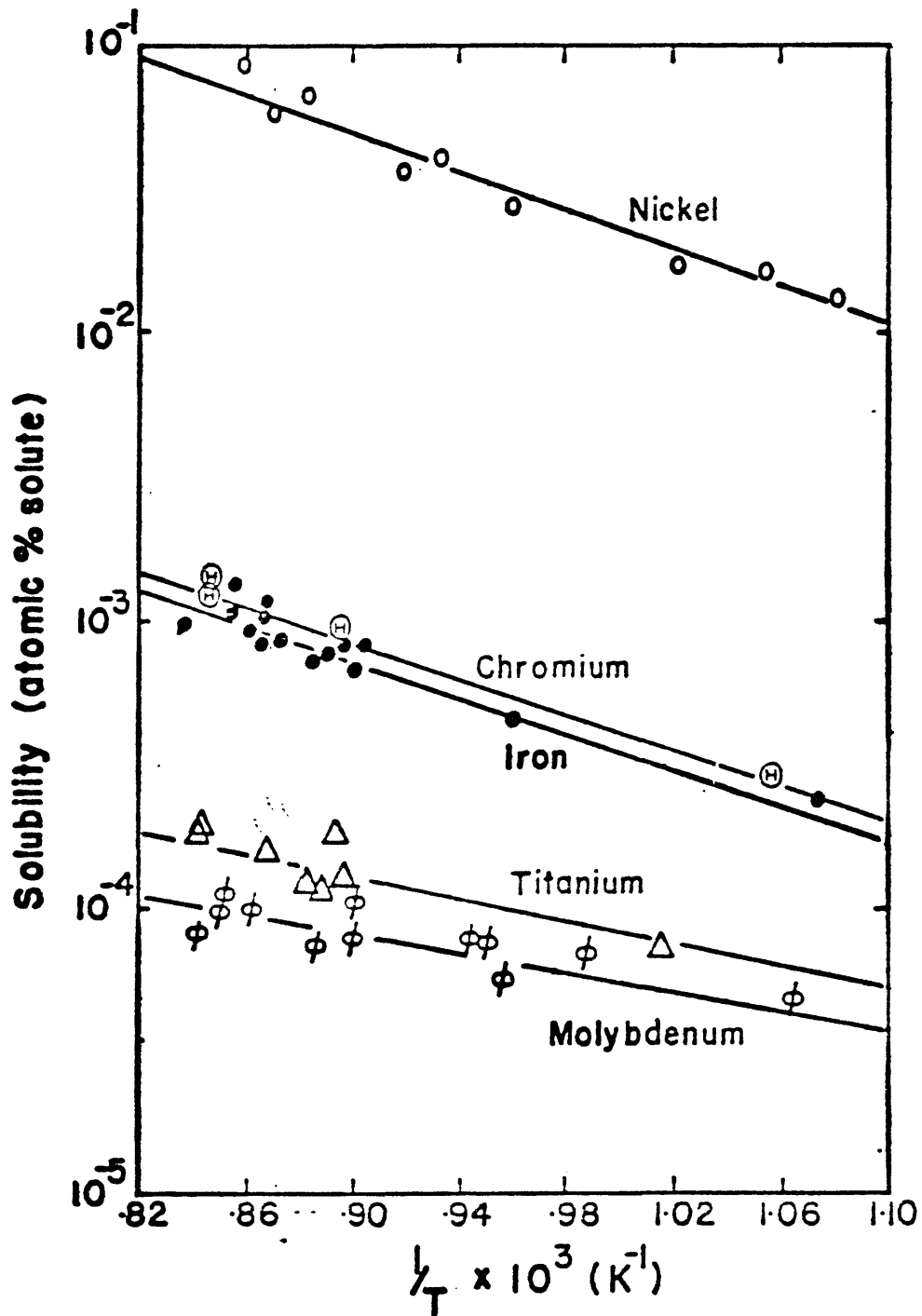


Figure 4. The temperature dependence of the solubilities of a number of metals. (52)

in liquid lithium has also been measured, (53)

$$\log_{10} (\text{at } \% \text{ Nb}) = -2.475 - \frac{1430}{T} \quad \text{eq. 1}$$

An important dissolution effect is caused by the wide range of metal solubilities. The high solubility of nickel over iron can lead to a leaching effect in austenitic stainless steels. (15,17,30,57) This type of behavior is very common in many corrosion systems. (10,15,17,26,37,58) If impurities are present in the alkali metals they can combine with the nickel and chromium in solution as compounds which upset the solubility equilibrium and promote further leaching. (37)

Impurity effects in simple solution are driven by both a modification of the solubility product (37) and compound formation, upsetting solubility equilibrium. (59) Solubility increases, resulting from impurities, have been observed in iron-bismuth, chromium-bismuth and liquid sodium-containment metal systems. In general, increasing the oxygen concentration in sodium or the nitrogen in lithium results in an increased solubility of iron, chromium, niobium and nickel. This is demonstrated in figure 5 for the titanium-lithium and niobium-lithium systems. (52) Equations 2 and 3 show impurity effects in the chromium-lithium and nickel-lithium systems. (56,59)

$$\text{Cr: } \log_{10} X = -2.1364 - 3.2193 \times 10^3 \frac{1}{T} \quad 150 \text{ ppm N}_2 \quad \text{eq. 2}$$

$$\log_{10} X = -1.1138 - 3.9096 \times 10^3 \frac{1}{T} \quad 790 \text{ ppm N}_2$$

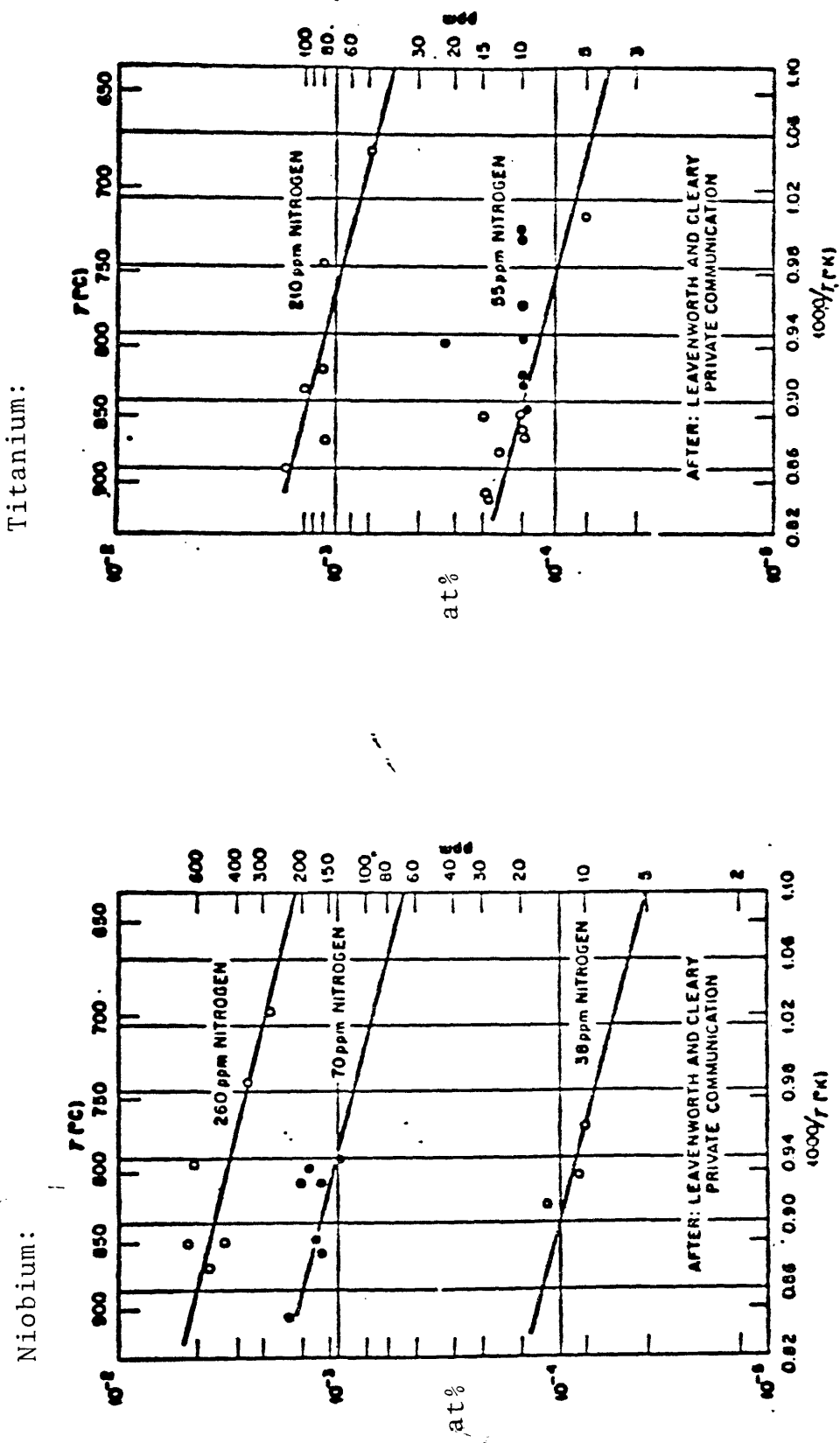


Figure 5. The solubility of niobium and titanium as a function of temperature and nitrogen concentration of liquid lithium. (52)

$$\text{Ni: } \log_{10} X = -0.2679 - 3.3642 \times 10^3 \frac{1}{T} \quad 146 \text{ ppm N}_2 \quad \text{eq. 3}$$

$$\log_{10} X = .3446 - 3.0020 \times 10^3 \frac{1}{T} \quad 220 \text{ ppm N}_2$$

The behavior known as uniform corrosion has been observed in many alkali-containment metal systems. (3,4,10,17,18,27,30,31,60-62) The alkali metal and impurities attack the surface directly forming scales. (18) Shown in figure 6 is the result of an impurity study upon uniform corrosion. (37) Increasing the impurity level results in an increased rate of corrosion. However, the impurities did not significantly alter the activation energy. Thus, the corrosion mechanisms are unchanged.

Alloying: Alloying between the liquid metal and solid metal, manifesting as a weight gain, occurs when the alkali metal diffuses into the container metal and forms a solid solution alloy. This type of behavior observed in the lithium-niobium system, (49,51) is diffusion controlled. Also lithium diffusion in iron alloys (63) and tantalum (60) has been shown. Lithium is soluble in copper and nickel. (64) When alloyed with other metals it forms a variety of intermetallic compounds with aluminum, bismuth, cadmium, calcium, cobalt, indium, lead, magnesium, mercury, silver, sodium, tin, and zinc. An example, the aluminum-lithium system, is given in figure 7. (65)

Impurities have an effect upon the diffusion of alkali metals in containment alloys. Shown in figure 8 are the

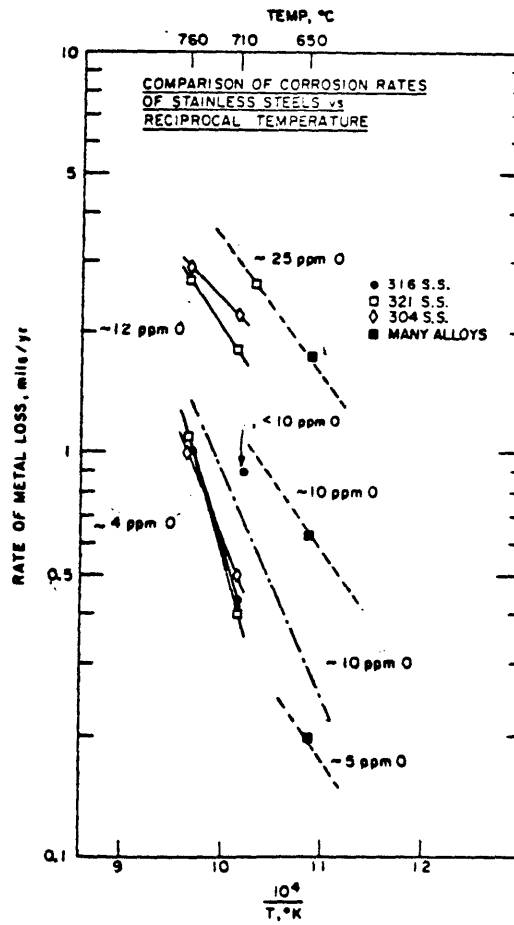


Figure 6. Comparison of the corrosion rates of stainless steel as a function of temperature and oxygen concentration of liquid sodium. (37)

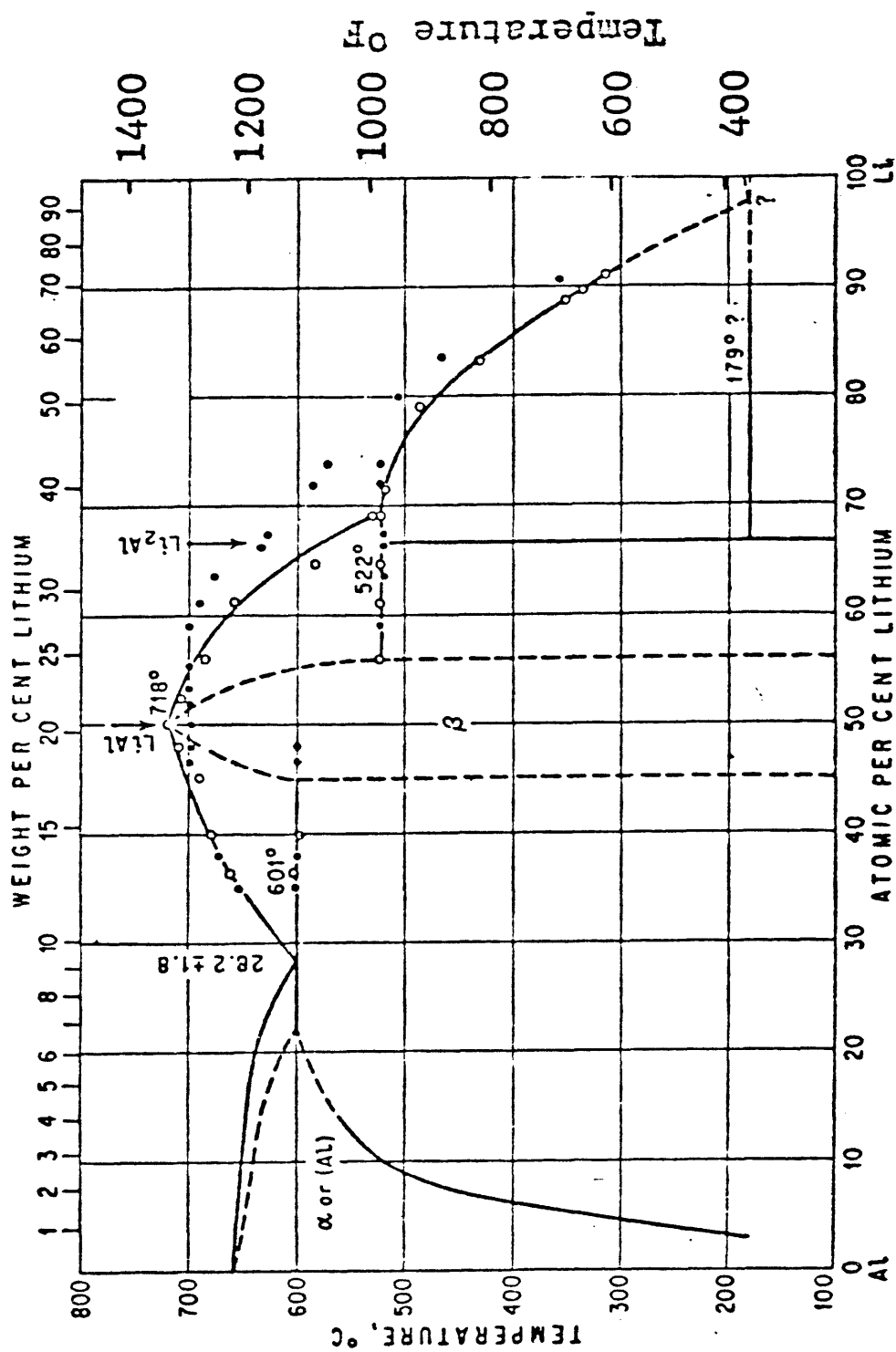


Figure 7. The lithium-aluminum equilibrium phase diagram determined by Lithium Corporation of America. (65)

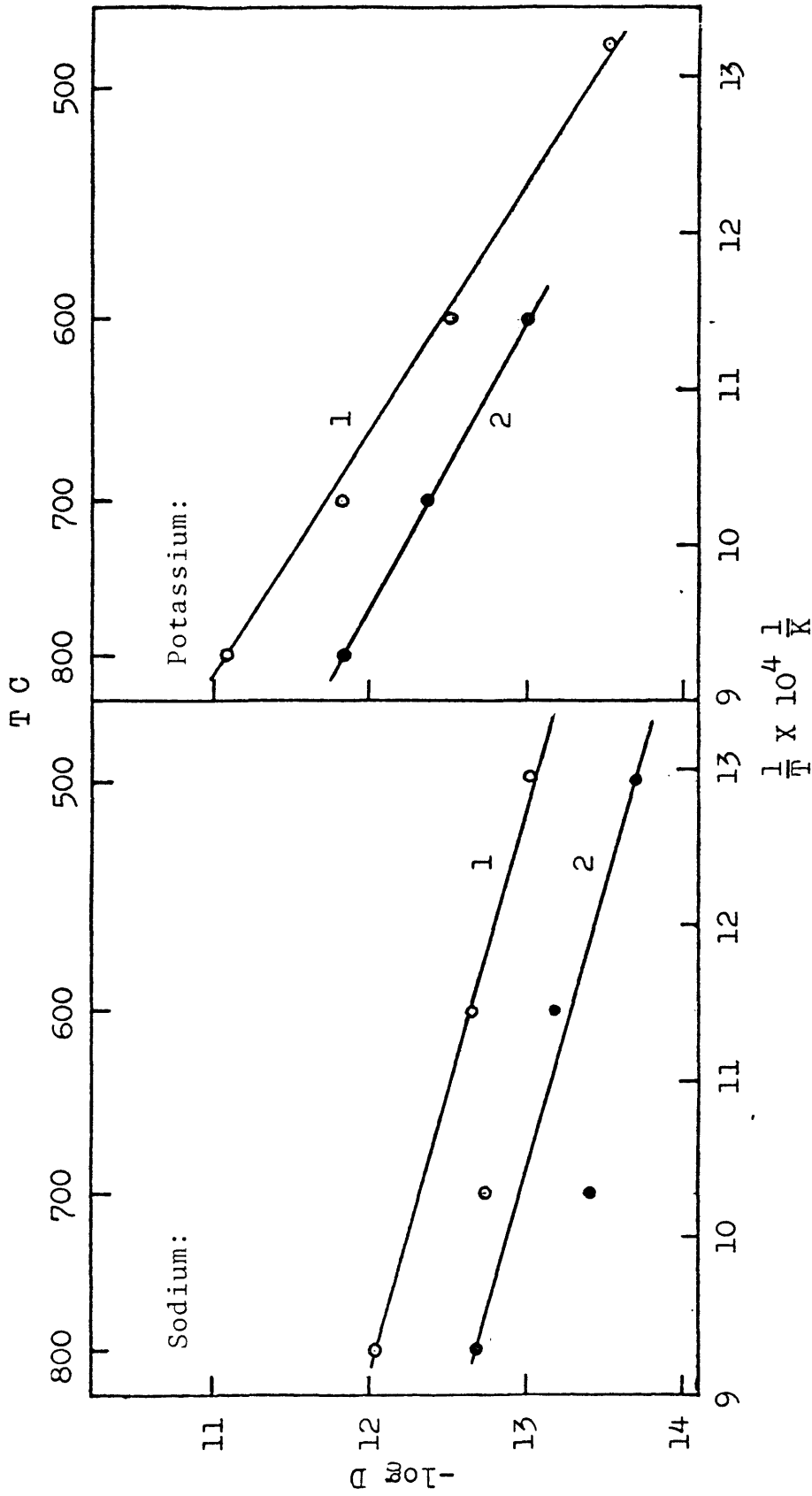


Figure 8. Temperature dependence of sodium and potassium diffusing into (1) Armco iron and (2) electrolytic iron. (36)

diffusion coefficients of sodium and potassium in pure iron.⁽³⁶⁾ It is important to notice the vital role interstitial impurities play. The diffusivity of sodium in Armco iron (.03 carbon) is greater than the diffusivity in electrolytic iron (.003 carbon). Realizing

$$D = D_0 \exp (-Q/RT) \quad \text{eq. 4}$$

it appears as if carbon, an impurity, increases the frequency factor, D_0 , but does not change the mechanism.

Intergranular Penetration: When a polycrystalline material is exposed to an alkali metal, one of the most common forms of corrosion is grain-boundary penetration. This type of containment metal-alkali metal interaction has been observed in a large variety of systems.^(2,29,37,40,45,48,50,61,67,69) There are two hypotheses put forth which explain selective attack upon a grain boundary:

- (1) In a given system differential free energies between the grain boundary and grain may act as a driving force for grain boundary penetration.⁽³⁷⁾
- (2) The grain boundary attack is due to the segregation and selective removal of certain constituents in the grain boundary region.^(14,40,61)

Niobium and tantalum are completely impervious to attack by pure alkali metals, except for a small initial dissolution.^(40,48,49,51) However, upon the addition of an interstitial impurity, oxygen, the refractory alloy is extremely susceptible

to intergranular attack. At a threshold level of 300 to 500 ppm oxygen in the refractory alloy, severe attack occurs.

(2,48,49,51) It was found that above 500 ppm the penetration increased with oxygen content. Figure 9 shows the oxygen impurity did not change the penetration mechanism, just the rate.

(48) The corrosion is caused by oxygen segregation at the grain boundary, reacting to precipitate a niobium-oxygen-lithium complex. Attempts to identify the compound by X-ray analysis indicated a rhombohedral unit cell but various known niobates of lithium failed to match the unknown pattern precisely. (51,49)

Segregation is observed in iron systems and promotes grain boundary penetration. (29,61,69) It has been observed in stainless steel systems that grain boundary attack is associated with chromium depletion. (61) A chromium-depleted boundary is surrounded by a nickel-rich alloy which is extremely susceptible to alkali attack. (40,47,61) Intergranular penetration (70) into armco iron proceeds by an attack on iron carbides located at the grain boundaries. Grain-boundary penetration caused by sensitization is even claimed in a 304-L-lithium system. (29) However, it is now thought the 304-L stainless steel was first carburized by the lithium.

In some corrosion systems intergranular attack is not due to segregation. (66,67,71) Grain-boundary attack in pure metals occurs by impurities diffusing from the alkali melt, along the penetrated boundary, to the active corrosion interface. (71,72)

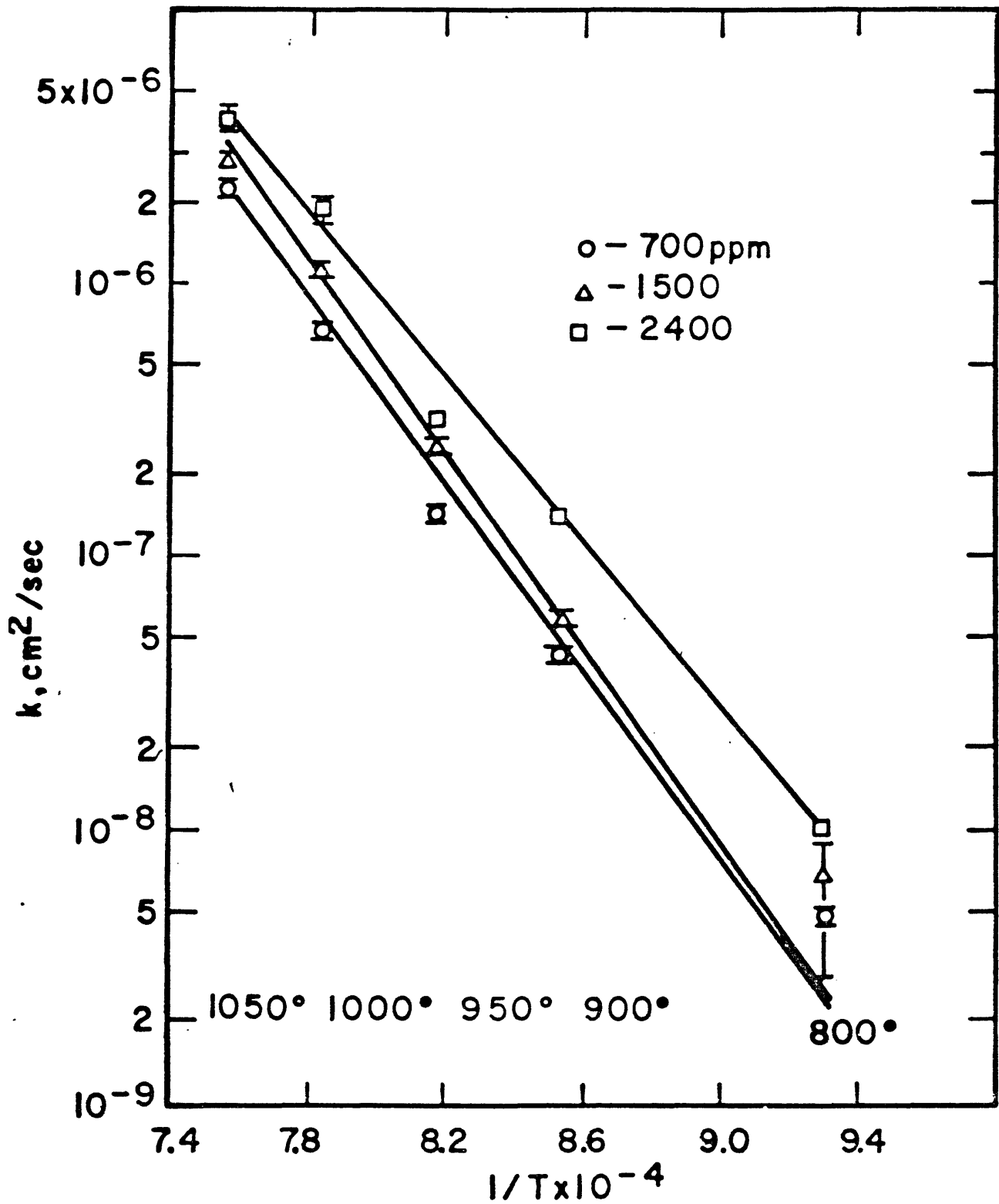


Figure 9. Arrhenius plot for grain boundary penetration into oxygen doped niobium by liquid lithium.⁽⁴⁸⁾

This effect has been studied by adding or regulating a known amount of contaminant to the lithium.^(40,67,71) Table IV shows the results of Li_3N contamination in a 316 stainless steel lithium system.⁽⁴⁰⁾ Also it has been proposed that grain boundary penetration will occur when twice the solid-liquid interfacial energy is less than the solid-solid grain-boundary energy.^(48,49) Thus it has been proposed segregation does not have to play any part at all in some penetration processes.

In several systems transgranular penetration of containment metals by liquid lithium has been observed.^(9,50,51,60,69) When oxygen exceeds the threshold level, attack occurs in tantalum and niobium along the (110) plane.⁽⁶⁰⁾ The same mechanisms discussed above are involved here.

Whether the penetration results from either one of the mechanisms above or both, it is not known how propagation occurs. Wedging by corrosion products or a simple chemical-dissolution attack may be responsible.^(60,34)

In samples supersaturated with impurities, interstitial diffusion is responsible for a penetration rate decrease.^(48,51,73) At high temperatures, the impurities diffuse out of the specimen reducing attack. This is observed in the niobium-oxygen-lithium and 316 stainless steel-nitrogen-lithium systems. Nitrogen loss from the 316 stainless system occurred at 50 hours and 871°C .⁽⁷³⁾

In some cases an incubation period is needed before penetration occurs.^(50,71) This delay is associated with the nucleation

TABLE IV. Li_3N EFFECTS ON THE CORROSION OF TYPE 316 STAINLESS STEEL IN LIQUID LITHIUM(40)

Test No.	Temperature		Lithium Nitride Addition to Lithium Weight Per Cent	Weight Change mg/in. ²	Metallographic Observations
	°F	°C			
1	1500	816	0.5	+ 2.4	8 mils of intergranular attack.
2	1500	816	1.0	- 12.3	35-mil tube wall completely penetrated intergranularly.
3	1500	816	2.0	7 1.0	35-mil tube wall completely penetrated intergranularly.
4	1600	871	0.1	0	35-mil tube wall completely penetrated intergranularly.
5	1600	871	0.25	- 4.0	35-mil tube wall completely penetrated intergranularly.
6	1600	871	1.0	- 14.8	35-mil tube wall completely penetrated intergranularly.

^aLithium nitride analysis: 58.4 Li - 37.1 N_2 - 1.5 CO_3 (weight per cent).

^bNitrogen content of lithium prior to addition of lithium nitride: 0.05 weight per cent.

time for the corrosion product or the time required for segregation. If the time needed to nucleate a metal carbide in a 316-L alloy (74) is compared with the delay observed in a 304-L-lithium system, (71) it is seen that the lapse is caused by corrosion product incubation. (See figure 10.)

Impurity Effects: In the corrosion systems examined, oxygen, nitrogen, and other impurities have accelerated attack. Oxygen and nitrogen, by increasing solubilities of containment materials, are partially responsible for intergranular penetration. Interstices reinforce alloy effects between containment and alkali metals by accelerating diffusion. Impurities also increase mass transfer in temperature and concentration gradients. (This last point will be discussed in detail later.)

The most important role nitrogen, oxygen and carbon impurities play is determining the chemical nature of the corrosion products. (10,18,26,37,38,50,51,61,75-78) This indicates the impurities are implicitly involved in the corrosion processes. Patterson (71) demonstrated the time needed for corrosion product nucleation, in a 304-L liquid lithium system, was a function of Li_3N phase stability. (65) (See figure 11).

Penetration of oxygen-doped niobium by lithium produces a niobium-oxygen-lithium complex. (48) Attempted analysis of this product shows a rhombohedral unit cell, but definite identification is pending. (51) However, it is a lithium niobate formation. (50) It is suggested that grain-boundary penetration

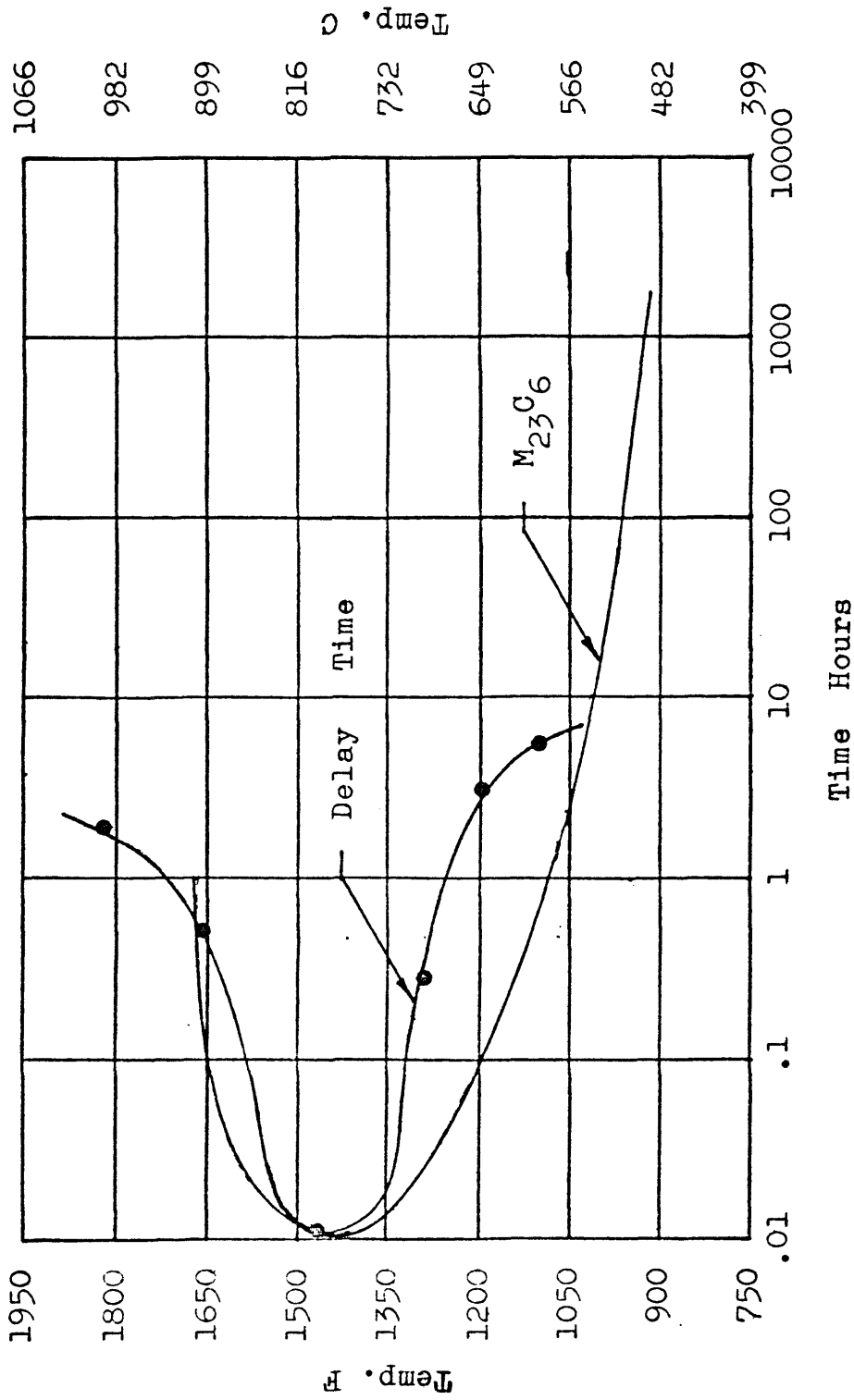


Figure 10. The time needed to nucleate a metal carbide in 316-L stainless steel compared with the delay time in a 304-L stainless steel-lithium system. (71,74)

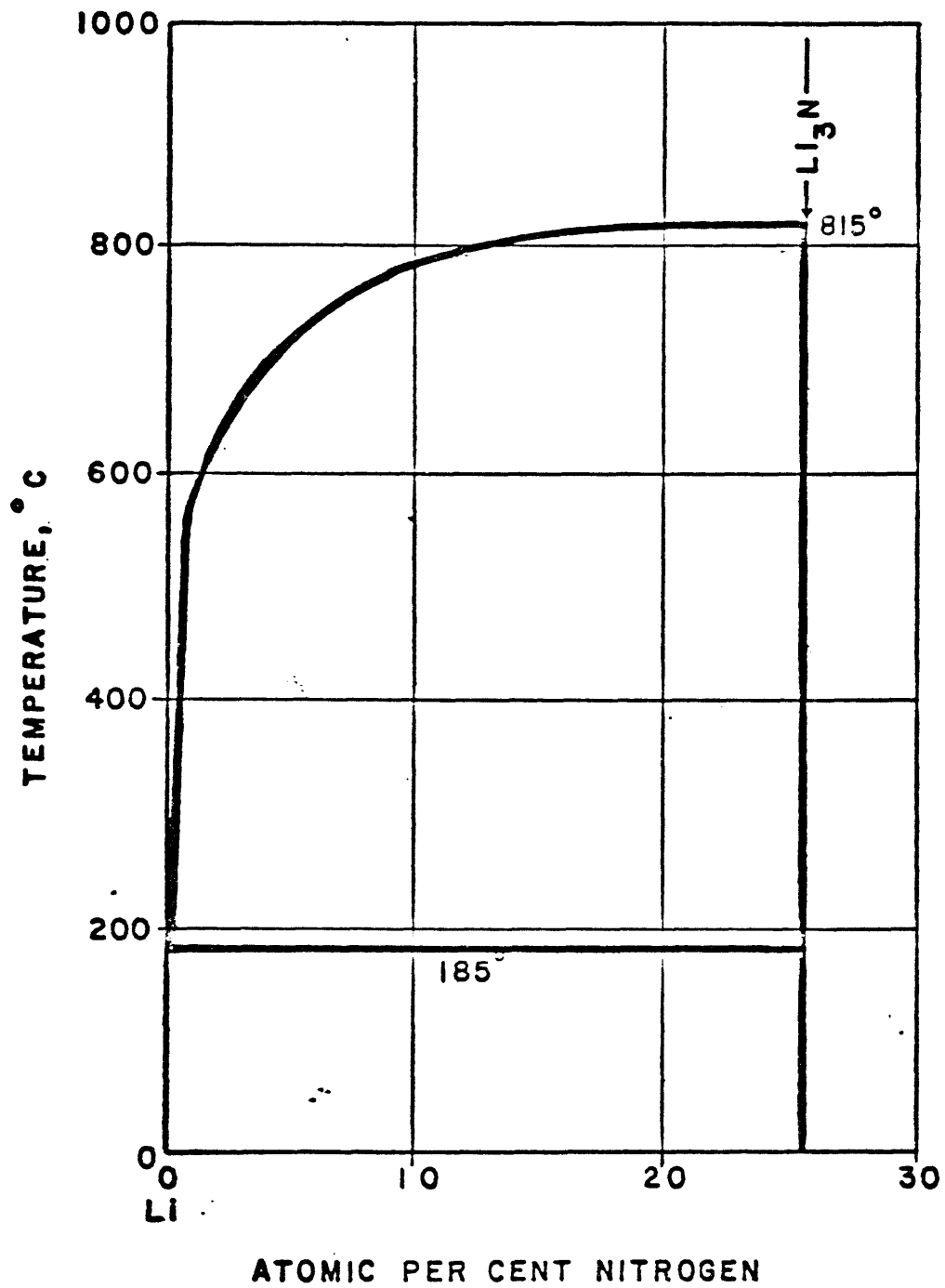


Figure 11. The Li_3N portion of the lithium-nitrogen equilibrium phase diagram. (65)

of tantalum by lithium results in a ternary oxide.⁽⁶⁰⁾ Sodium and potassium interactions involving oxygen react with refractory metals in a similar manner.⁽⁹⁾ It is reported that the corrosion products $K_4Nb_6O_{17}$, K_3NbO_4 , and $NaNbO_3$ have been isolated in these systems.⁽⁷⁶⁾

Iron alloy-alkali corrosion interactions have been studied. In stainless steel systems interacting with lithium, $CrNLi_3N$ compounds are thought to exist.⁽⁶¹⁾ A compound, Li_3NFeN is postulated in a stainless steel-nitrogen-lithium system.⁽⁴⁰⁾ The attack of iron carbides in iron by lithium forms a L_2C_2 product.^(69,70,75) In the analogous sodium-iron alloy systems a wide variety of complex corrosion products are observed. $(Fe,Cr,Ni)_{23}C_6$, $(Fe,Cr,Ni)C_3$ are found along with minor amounts of $Na(Fe,Cr,Ni)O_2$ in flowing non-isothermal loops.^(26,78) Trace amounts of α - $NaFeO_2$ and $NaNiO_2$ were also seen. The corrosion of pure iron proceeds by the formation of $(Na_2O)FeO$.⁽¹⁸⁾ In stainless steel loops $Na_2O \cdot Cr_2O_3$ is a corrosion product.⁽¹⁰⁾ Manganese leaching in steels is associated with $NaMnO_4$ while sodium interacts with silicon in steel to form a $Na_2O \cdot SiO_2$ - (Na_2SiO_3) complex.

In niobium-oxygen-lithium systems the corrosion compound exhibits a solid-to-liquid transition at $1100^\circ C$.^(48,79) Lithium carbide also has a similar behavior.⁽⁷⁰⁾

The formation chemistry for the corrosion compounds is not completely understood; however, nitrogen and oxygen do play an

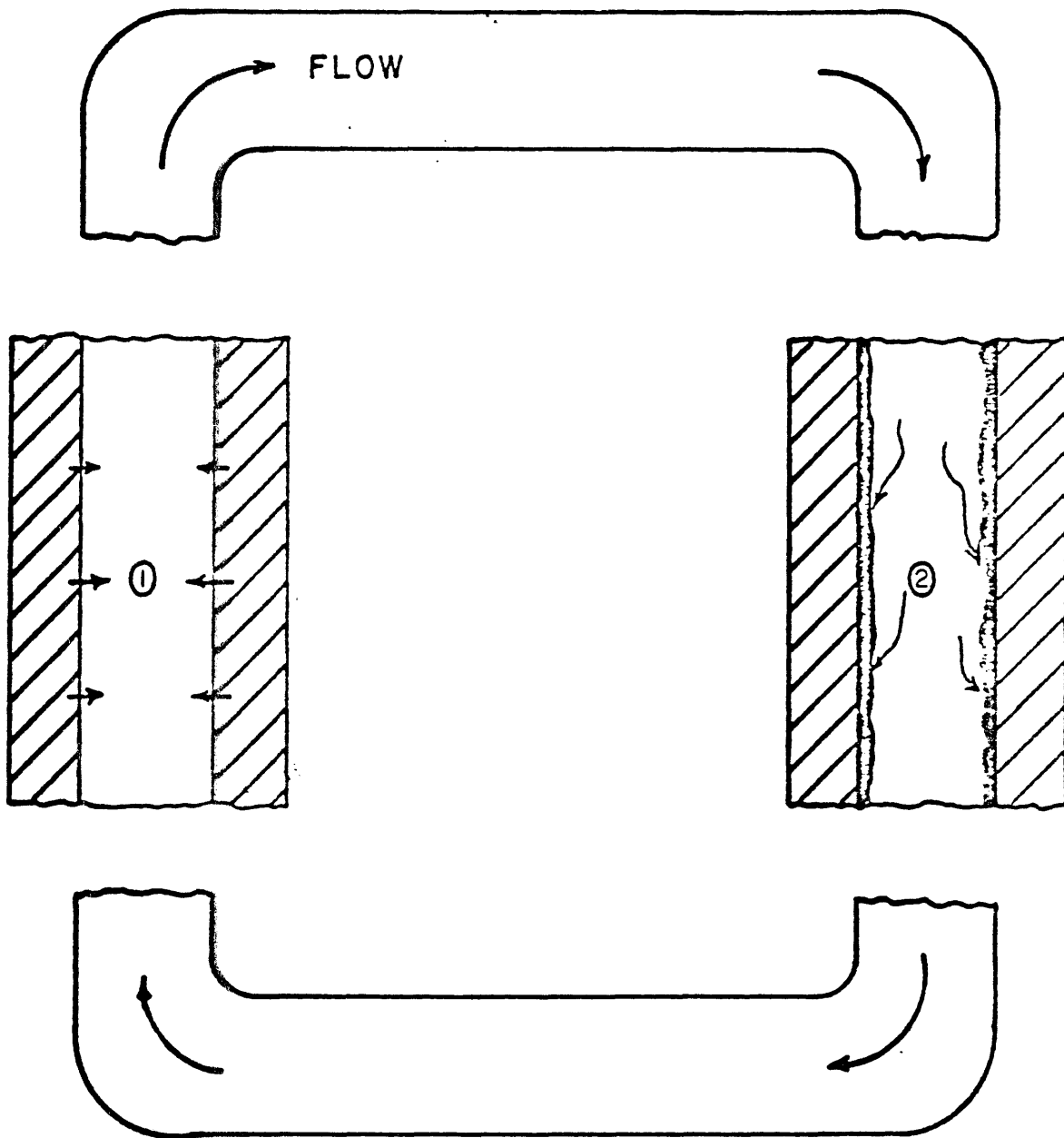
important role. Even the best identified compounds, determined by X-ray analysis, have anomalous unknowns.⁽¹⁸⁾

Temperature Gradient Mass Transfer: When an alkali metal-containment metal system experiences non-isothermal flowing conditions, many investigators have reported an increase in the corrosion rate.^(1,4,5,17,26,29,30,37,38,58,69) Figure 12 is a conceptual heat-exchanger loop illustrating a temperature gradient dissolution-deposition process.⁽⁴⁰⁾ Solubility equilibrium in the hot zone, between the soluble corrosion products and containment-metal alloys, has been achieved. However, the cold zone decreases solubility and deposition occurs. In flowing sodium systems the transport rate depends upon the dissolved alloy species.⁽¹⁾ Other variables include contamination, temperature difference, and velocity effects. Corrosion and deposition, increasing functions of velocity⁽³⁷⁾ and temperature difference,⁽²⁶⁾ depend upon the carbon and oxygen contents in the coolant.^(10,75) In lithium loops mass transfer increases with velocity,⁽⁴⁰⁾ impurities,⁽⁶⁶⁾ and temperature difference.⁽²⁶⁾

The deposition-dissolution process is controlled by the deposition rate in the cold leg.^(26,37) Thus a possible failure will be caused by a constriction in the cold zone.^(26,58,69)

Dissimilar Metal Effects: Mass transport in alkali-metal systems is caused by dissimilar metals or concentration gradients. (See figure 13.) Transport caused by alloy concentrations^(7,15,21,35,80,81) has been observed by a number of

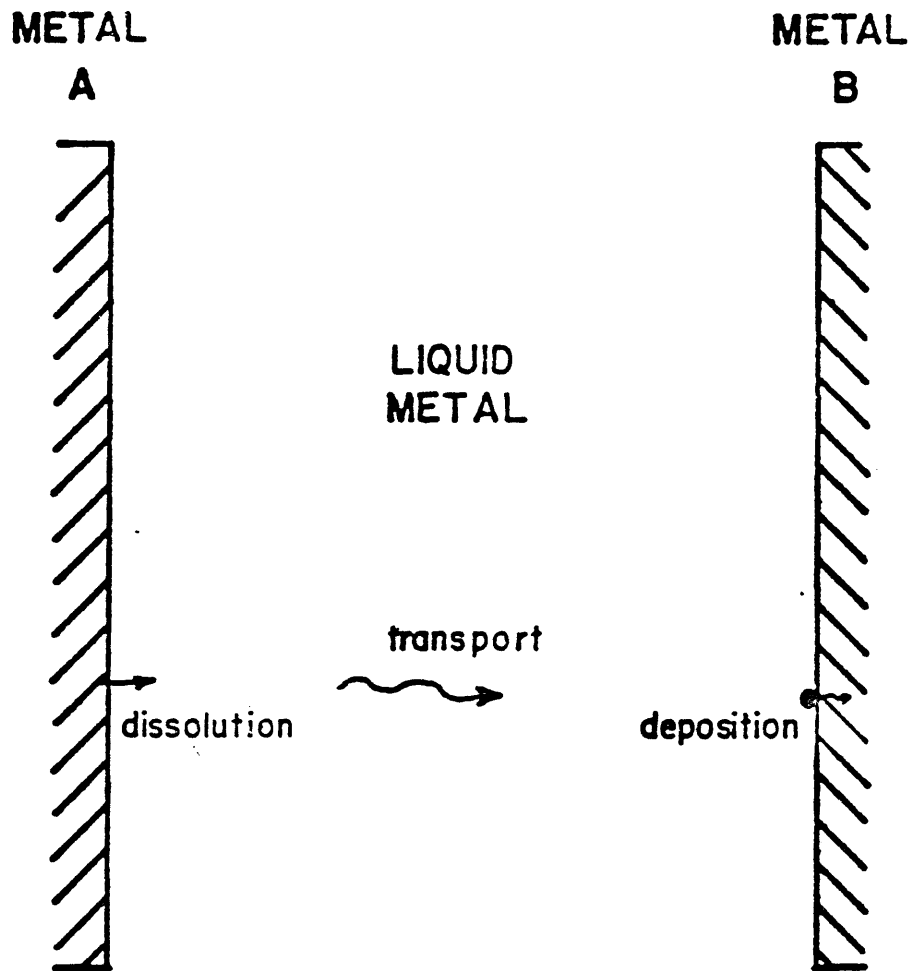
TEMPERATURE GRADIENT MASS TRANSFER



1- HOT ZONE dissolution process

2- COLD ZONE deposition process

Figure 12. A schematic diagram of the concept of a loop containing flowing liquid metal in the presence of temperature gradients. (40)



DISSIMILAR METAL EFFECTS

Figure 13. A schematic diagram showing the mass transport possible in the presence of dissimilar metals or concentration gradients. (71)

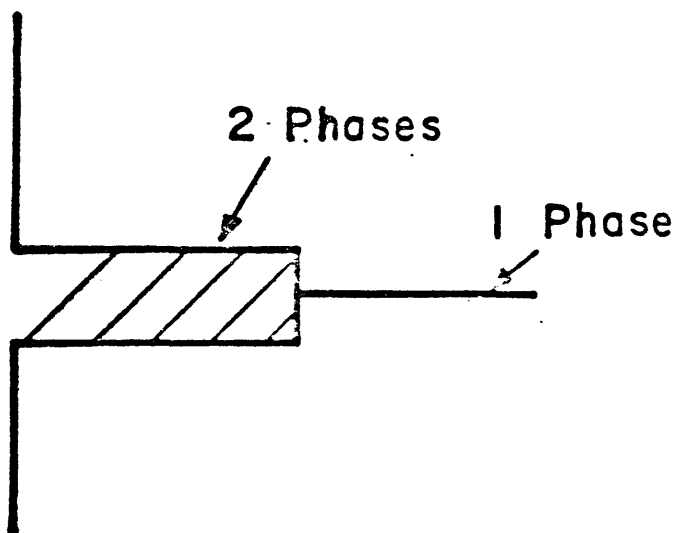
experimenters. (7,21,35,57,66,81) Transport of vanadium from vanadium alloys to 321 stainless steel is observed in sodium loops. (57) In a similar manner nickel moves through sodium and deposits upon molybdenum. (40) Mass transfer of carbon, resulting in carburization-decarburization, has been observed between different grades of steel. (7,21,35)

Dissimilar metal transfer is an increasing function of temperature, (69) exposure time, and impurity (75) content in liquid lithium. (15,50) Concentration gradient transfer is important since the cooling circuits for reactors are constructed from several different materials

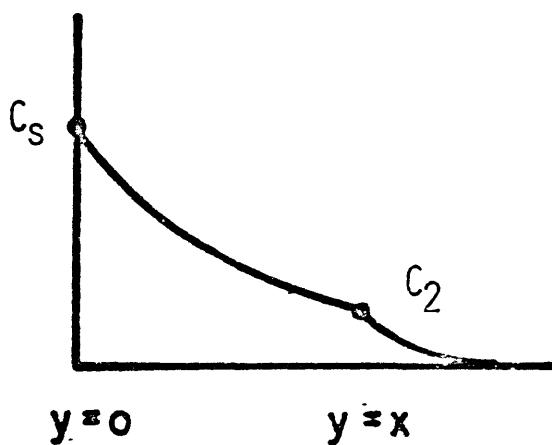
There are many theories explaining alkali corrosion. (7,13,15,21,22,23,34,37,38,48,49,71) However, it is not appropriate to present a comprehensive review; rather, only two pertinent theories will be discussed in detail. These deal directly with the grain-boundary penetration of liquid lithium into an alloy.

Theoretical Presentation by Brehm: In the following analysis taken from Brehm (48,49) the penetrated grain boundary of a niobium bicrystal (see figure 14) is assumed to be a solid and to consist of a two-phase region. The phases are a solid solution of niobium, oxygen, and lithium plus a precipitated (Nb-O-Li) complex. The zone in front of the penetrated boundary is a single solid solution phase of niobium, oxygen, and lithium.

The following assumptions are made about the corrosion system:



(a) Penetrated Zone



(b) Concentration Profile of Lithium

Figure 14. Penetrated zone and concentration profile as assumed by Brehm. (48,49)

- (1) The diffusion of lithium is entirely through the solid solution phase. Thus D is the diffusion coefficient of lithium in the grain-boundary region.
- (2) D is independent of position.
- (3) Local equilibrium exists for all places at all times.
- (4) Oxygen migration does not influence the rate of advance of the penetrated zone.

In figure 14, the interface between the penetrated and nonpenetrated region is at $y = x$. The lithium concentration is C and the boundary conditions are:

$$\begin{aligned} \text{B.C.} \quad C &= 0 && \text{at } y > 0 \text{ and } t = 0 \\ C &= C_S && \text{at } y = 0 \text{ and } t > 0 \\ C &= C_2 && \text{at } y = x \text{ and } t > 0 \end{aligned}$$

Using the diffusion equation for the interval $0 < y < x$

$$D \frac{\partial^2 C}{\partial y^2} = \frac{\partial C}{\partial t} \quad \text{eq. 5}$$

the appropriate solution is:

$$C = C_S - \text{Aerf} \left(\frac{y}{\sqrt{4Dt}} \right) \quad \text{eq. 6}$$

Given C_A is the average concentration of lithium in the niobium between $y = 0$ and $y = x$, equation 7 follows from a mass balance.

$$-D \left. \frac{\partial C}{\partial y} \right|_{y=0} = C_A \frac{dx}{dt} \quad \text{eq. 7}$$

Upon combining equations 6 and 7 the following condition is found:

$$A \sqrt{\frac{D}{\pi t}} = C_A \frac{dx}{dt} \quad \text{eq. 8}$$

The solution to equation 8 is

$$x = \sqrt{Kt} \quad \text{eq. 9}$$

provided

$$\sqrt{K} = \sqrt{\frac{4D}{\pi}} \frac{A}{C_A} \quad \text{eq. 10}$$

The boundary conditions, $C = C_2$ and $y = x$, with equations 6 and 9 yield

$$C_2 = C_S - A \operatorname{erf} \sqrt{\frac{K}{4D}} \quad \text{eq. 11}$$

where

$$A = \frac{C_S - C_2}{\operatorname{erf} \left(\sqrt{\frac{K}{4D}} \right)} \quad \text{eq. 12}$$

The final solution for $0 < y < x$ is

$$C = C_S - \left(\frac{C_S - C_2}{\operatorname{erf} \sqrt{\frac{K}{4D}}} \right) \operatorname{erf} \left(\frac{y}{\sqrt{4Dt}} \right)$$

where K is a constant to be determined.

To find K, equation 12 and 10 are used

$$\sqrt{\frac{\pi K}{4D}} \operatorname{erf} \sqrt{\frac{K}{4D}} = \frac{C_S - C_2}{C_A} \quad \text{eq. 13}$$

If the lithium and oxygen interact on a one-to-one basis in the precipitate then, $C_A = V$, where V is the original concentration in the grain boundary. Provided the solid solubility of lithium, $C_S - C_2$, is less than the amount of lithium present, C_A , then $4D > K$ and equation 13 becomes

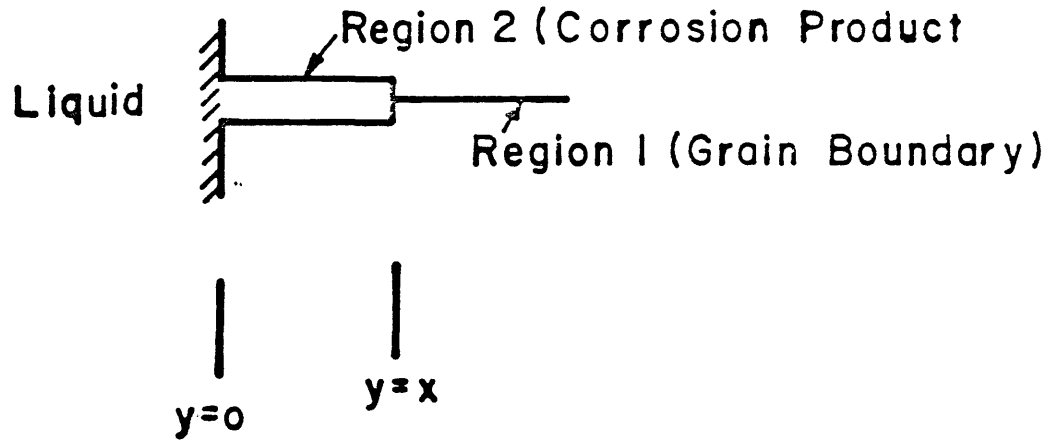
$$2 \left(\frac{K}{4D} \right) - \frac{2}{3} \left(\frac{K}{4D} \right)^3 + \frac{1}{5} \left(\frac{K}{4D} \right)^5 + \dots = \frac{C_S - C_2}{C_A}$$

or

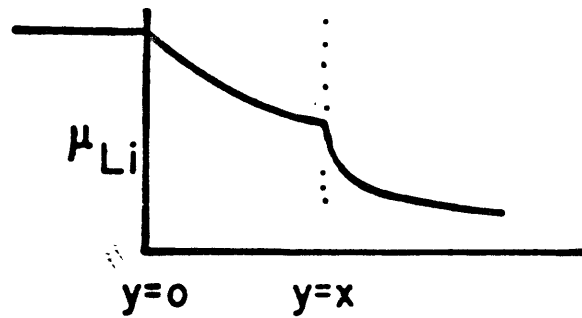
$$K = 2D \left[\frac{C_S - C_2}{C_A} + \frac{1}{3} \left(\frac{C_S - C_2}{C_A} \right)^2 + \dots \right] \quad \text{eq. 14}$$

If the values of C_S , C_2 , D and C_A were known as a function of temperature, the penetration could be calculated. The emphasis of the above model is the rate is parabolic and depends on K. But K is a function of D, the diffusion coefficient of lithium in the two-phase region. Also this theory could be applied to other systems with a minimal number of changes.

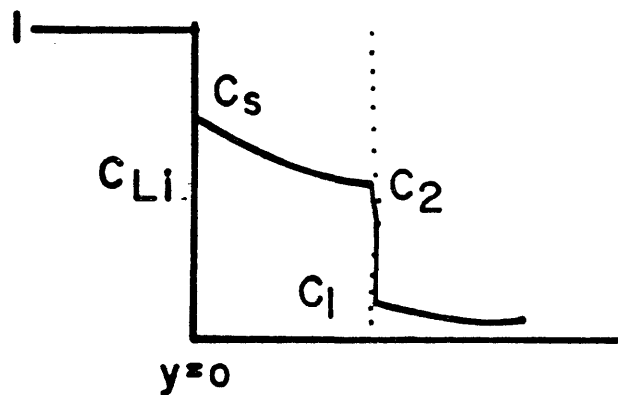
Theoretical Presentation by Patterson: Patterson⁽⁷¹⁾ describes the grain-boundary penetration of lithium into a 304-L stainless steel. Given the penetrated specimen (see figure 15), region 2 has two phases: A (Li-Me-N) complex plus austenite. Region 1, a lithium solid solution in austenite, is a single-phase system.



(a) Liquid & Penetration Zone



(b) Chemical Potential of Lithium



(c) Concentration of Lithium

Figure 15. Penetration zone, chemical potential profile, and concentration profile as assumed by Patterson. (71)

The chemical potential, in figure 15, is established by diffusion. At the sample's surface the constant-chemical potential is μ_{Li} , the chemical potential at the reaction interface, is also constant. Likewise the corresponding concentrations are shown in figure 15. To solve this problem the following assumptions must be made:

- (1) D_1 and D_2 are the respective diffusivities of lithium in region 1 and region 2.
- (2) The conditions of local equilibrium are satisfied at all times for the interfaces. The interfacial concentrations of lithium are C_S , C_2 , and C_1 .
- (3) The reaction interface has the coordinate x .

A mass balance, $0 < y < x$, requires

$$(C_2 - C_1) \frac{dx}{dt} = -D_2 \left. \frac{\partial C}{\partial y} \right|_{y=x^-} + D_1 \left. \frac{\partial C}{\partial y} \right|_{y=x^+} \quad \text{eq. 15}$$

Using the diffusion equations and boundary conditions,

$$D_2 \frac{\partial^2 C}{\partial y^2} = \frac{\partial C}{\partial t} \quad y < x \quad \text{eq. 16}$$

$$D_1 \frac{\partial^2 C}{\partial y^2} = \frac{\partial C}{\partial t} \quad y > x \quad \text{eq. 17}$$

B.C.

$$\begin{aligned} C &= C_S, & y &= 0, & t &> 0 \\ C &= C_2, & y &= x^-, & t &> 0 \\ C &= C_1, & y &= x^+, & t &> 0 \\ C &= 0, & y &> 0, & t &= 0 \\ C &= 0, & y &= \infty, & t &> 0 \end{aligned}$$

the solution to equations 16 and 17 are

$$C = C_S - A \operatorname{erf} \frac{y}{\sqrt{4D_2 t}} \quad y < x \quad \text{eq. 18}$$

$$C = B(1 - \operatorname{erf} \frac{y}{\sqrt{4D_1 t}}) \quad y > x \quad \text{eq. 19}$$

with A and B as constants. If equations 18 and 19 are used in equation 15, the result is

$$(C_2 - C_1) \frac{dx}{dt} = \frac{D_2 A}{\sqrt{\pi D_2 t}} \exp\left(\frac{-x^2}{4D_2 t}\right) - \frac{D_1 B}{\sqrt{\pi D_1 t}} \exp\left(\frac{-x^2}{4D_1 t}\right) \quad \text{eq. 20}$$

The final solution, extracted by dimensional analysis, becomes

$$x = \sqrt{Kt} \quad \text{eq. 21}$$

However, A, B, and K still remain undetermined, thus combining equations 21 and 20, the result is

$$(C_2 - C_1) \sqrt{K} = \sqrt{\frac{4D_2}{\pi}} A \exp\left(\frac{-K}{4D_2}\right) - \sqrt{\frac{4D_1}{\pi}} B \exp\left(\frac{-K}{4D_1}\right) \quad \text{eq. 22}$$

From the boundary conditions, ($y = x^-$, $C = C_2$; $y = x^+$, $C = C_1$), equation 18, equation 19, and equation 21, A and B are determined.

$$A = \frac{C_S - C_2}{\operatorname{erf} \sqrt{K/4D_2}} \quad B = \frac{C_1}{1 - \operatorname{erf} \sqrt{K/4D_1}} \quad \text{eq. 23}$$

Substituting A and B into equation 22, a relationship for K appears

$$(C_2 - C_1)\sqrt{K} = \sqrt{\frac{4D_2}{\pi}} (C_S - C_2) \frac{\exp(-K/4D_2)}{\operatorname{erf}\sqrt{K/4D_2}} - \sqrt{\frac{4D_1}{\pi}} C_1 \frac{\exp(-K/4D_1)}{(1 - \operatorname{erf}\sqrt{K/4D_1})} \quad \text{eq. 24}$$

Provided $D_2 \gg D_1$, or C_1 is small, the right term in equation 24 is neglected.

$$\sqrt{\frac{K\pi}{4D_2}} \operatorname{erf}\sqrt{\frac{K}{4D_2}} \exp\left(\frac{K}{4D_2}\right) = \frac{C_S - C_2}{C_2 - C_1} \quad \text{eq. 25}$$

If further assumption permits, $(C_S - C_2) < (C_2 - C_1)$ or $4D_2 > K$, then

$$2\left(\frac{K}{4D_2}\right) + \frac{4}{3}\left(\frac{K}{4D_2}\right)^2 - \frac{1}{8}\left(\frac{K}{4D_2}\right)^3 + \dots = \frac{C_S - C_2}{C_2 - C_1} \quad \text{eq. 26}$$

equivalently

$$K = 2D_2 \left[\left(\frac{C_S - C_2}{C_2 - C_1}\right) - \frac{1}{3}\left(\frac{C_S - C_2}{C_2 - C_1}\right)^2 + \dots \right] \quad \text{eq. 27}$$

A parabolic rate is predicted, which depends on a constant K . K is a function of D_2 , the diffusion coefficient for lithium in the two-phase region.

The two models by Brehm and Patterson are essentially the same. However, the work from Patterson⁽⁷¹⁾ is more general since it allows for concentration discontinuities at the phase boundaries. The continuity condition imposed by Brehm^(48,49) could be described by Patterson as $C_S - C_2 \gg C_2 - C_1 \approx 0$. The general solutions from Brehm, equations 9 and 13, and Patterson, equations 21 and 24, were solved in closed form, equations 14

and 27, by making certain limiting assumptions. Brehm permitted $C_S - C_2 < C_A$ while Patterson let $C_S - C_2 < C_2 - C_1$. Thus the two theories do have subtle differences.

Uniform Corrosion Theory: A dissolution attack is controlled by the diffusion of alloy elements out of the sample into the liquid metal.^(38,40) This process in a static isothermal system attempts to meet the solubility requirements for equilibrium. Since attack is diffusion controlled it is again expected to be parabolic. Thus

$$\frac{\text{weight loss}}{\text{unit surface area}} = \sqrt{Kt}$$

where K is a temperature-dependent constant.

OBJECTIVES

The objective of this research effort was to investigate the effects nitrogen doping has on grain-boundary penetration in a 304-L stainless steel-liquid lithium environment. Nitrogen action in the static-isothermal environment was studied by comparing the specimen reactions to a previously prepared 304-L stainless steel-liquid lithium standard.⁽⁷¹⁾ The results will develop, define, and clarify an intergranular penetration model.

EXPERIMENTAL PROCEDURE

Materials

The lithium, 99.9% pure, was shipped under mineral oil in stainless steel containers. The .635 cm diameter rods, 12 inches long, were purchased from the Research Organic-Inorganic Chemical Corporation. The as-received lithium was covered with a black lithium nitride scale.

Since previous work (71) was used as a control, the 304-L samples used in this investigation were prepared with a similar grain structure. This was necessary because grain boundary penetration is affected by grain size, (84).

The proper nitriding procedure was determined by first rolling a .075 inch 304-L sheet to .055 inches followed by a 1100° C, 4-hour anneal in a NH₃ atmosphere. Diffusion coefficients in a similar alloy (18Cr, 12Ni) (as shown in figure 16) for an ammonia atmosphere indicated 3.8 hours produced .21 wt % nitrogen saturation. (82) The nitrided specimens were then worked to .035 inch. At 1100° C, in an ammonia atmosphere, a grain growth curve, see figure 17, was constructed. The time required for Patterson's (71) grain size, .0449 mm was 8 minutes. The remaining samples were annealed for 8 minutes. The nitred microstructure, figure 18, had an actual size of .454 millimeters. (83)

Apparatus

A stainless steel glove box maintained the test environment. The box, filled with 99.98% argon, had a positive differential

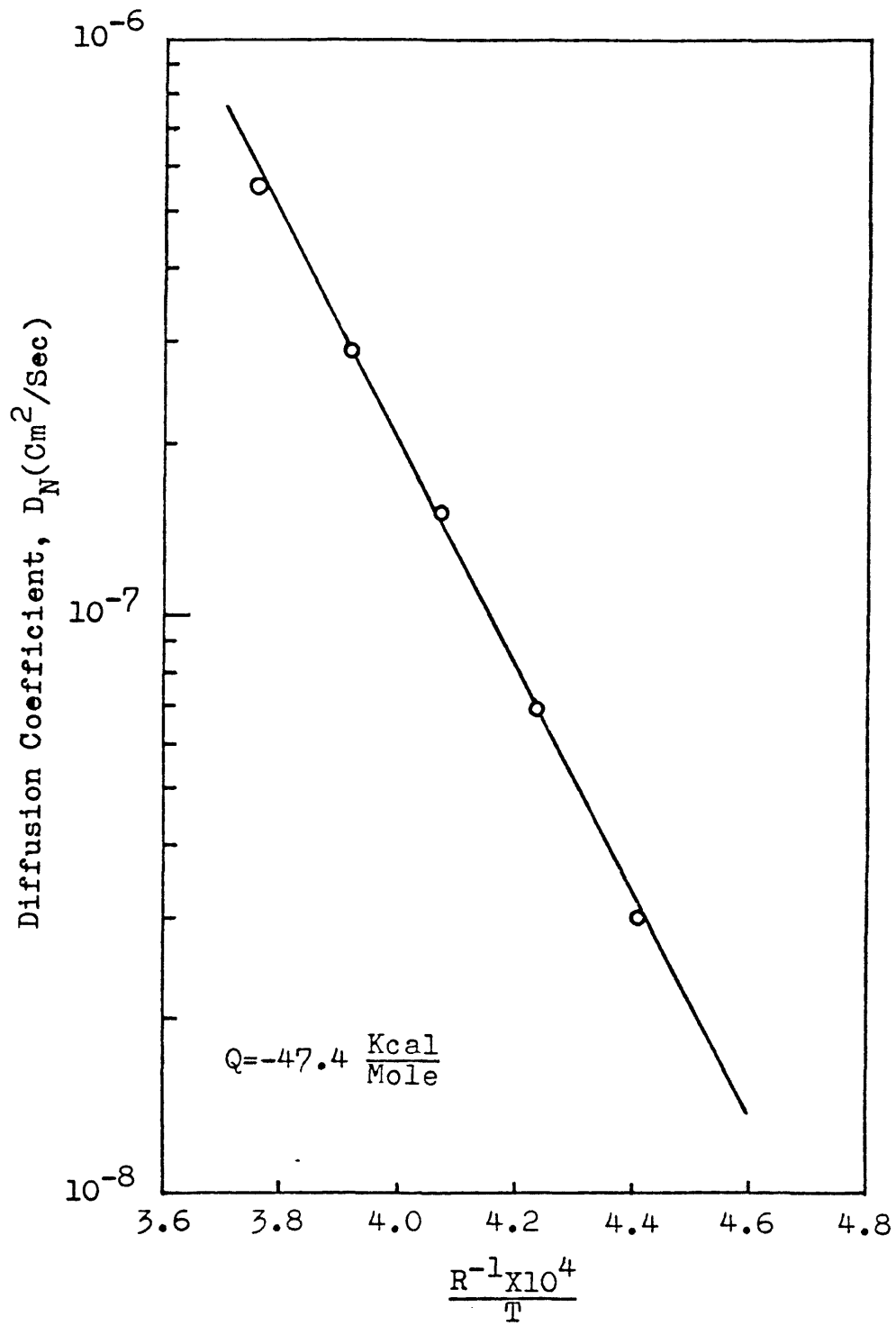


Figure 16. Nitrogen diffusion in an 18% chromium, 12% nickel, iron alloy. (82)

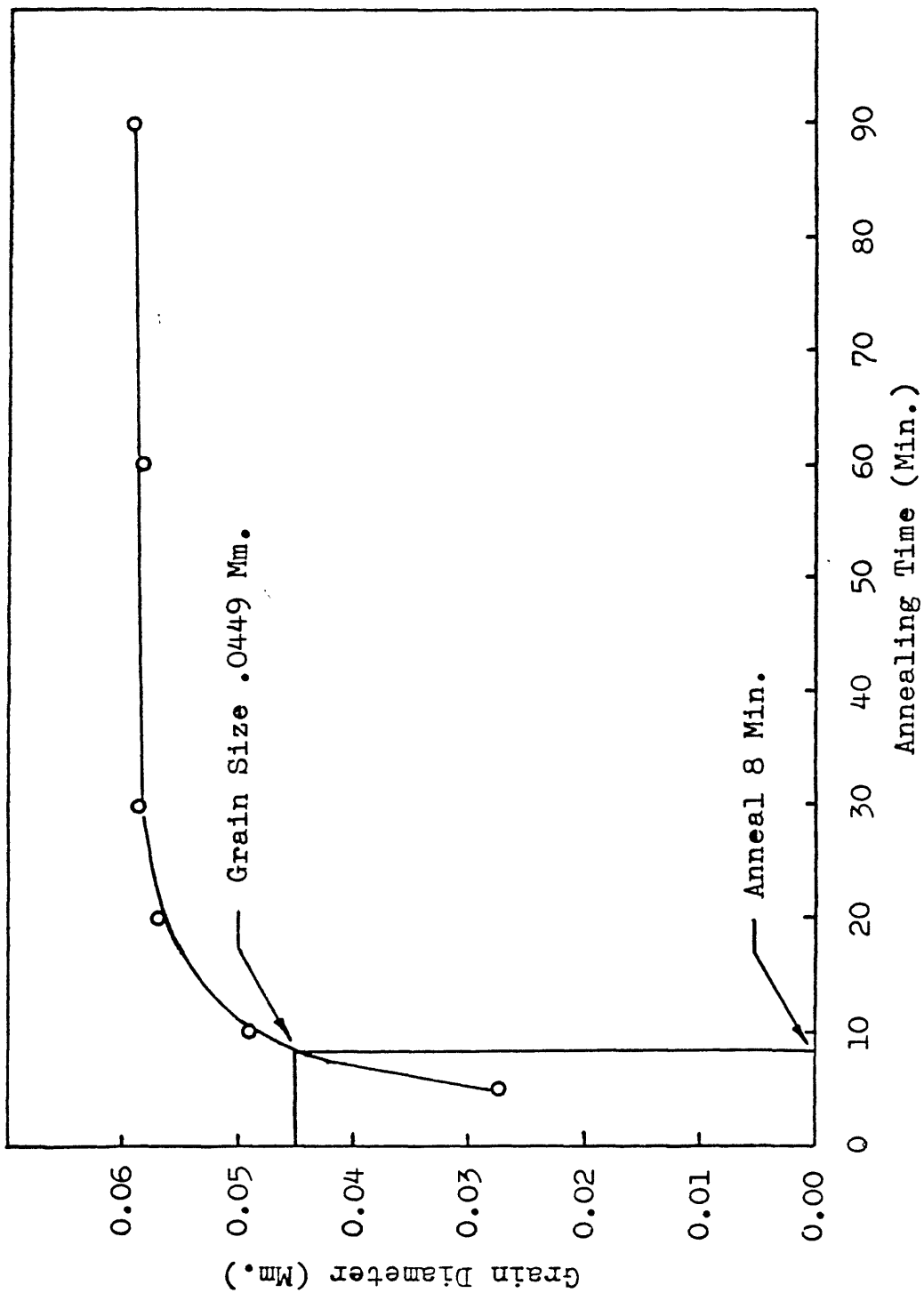


Figure 17. Grain growth curve at 1100° C for annealing 304-L stainless steel in an ammonia atmosphere.



Figure 18. A photo-micrograph showing the as annealed nitrided microstructure. X 100

pressure of .4 inch H_2O . The atmosphere in the box was oxygen gettered by a stirring flask of eutectic NaK (sodium-potassium). All incoming gas was bubbled through a similar eutectic NaK solution. The NaK surface, maintaining oxygen contamination at a minimal level, was continuously free from oxides during tests.

Nitrogen control in the environment was facilitated by lithium nitride equilibrium. A lithium nitride surface scale, indicating nitrogen saturation, was seen each time the test crucible was opened. However, lithium nitride was not seen above $812^{\circ}C$ since this species is unstable. (See figure 11.)

Figure 19, the test crucible and furnace, shows dissimilar metal effects are minimized by complete construction of the crucible with 304-L stainless steel. Up to 20 samples were suspended from the removable lid with no sample-sample interactions becoming evident. The specimens were suspended with pure iron wire. In all the tests conducted no preferential removal or plating was observed, thus bimetal effects were considered negligible.

The lithium was located in the center of the hot zone. Thus temperature fluctuations were minimized by the position of the lithium and its high thermal conductivity. The furnace, controlled by a Marshall 4044 proportional controller, provided temperature control to $\pm 2^{\circ}C$.

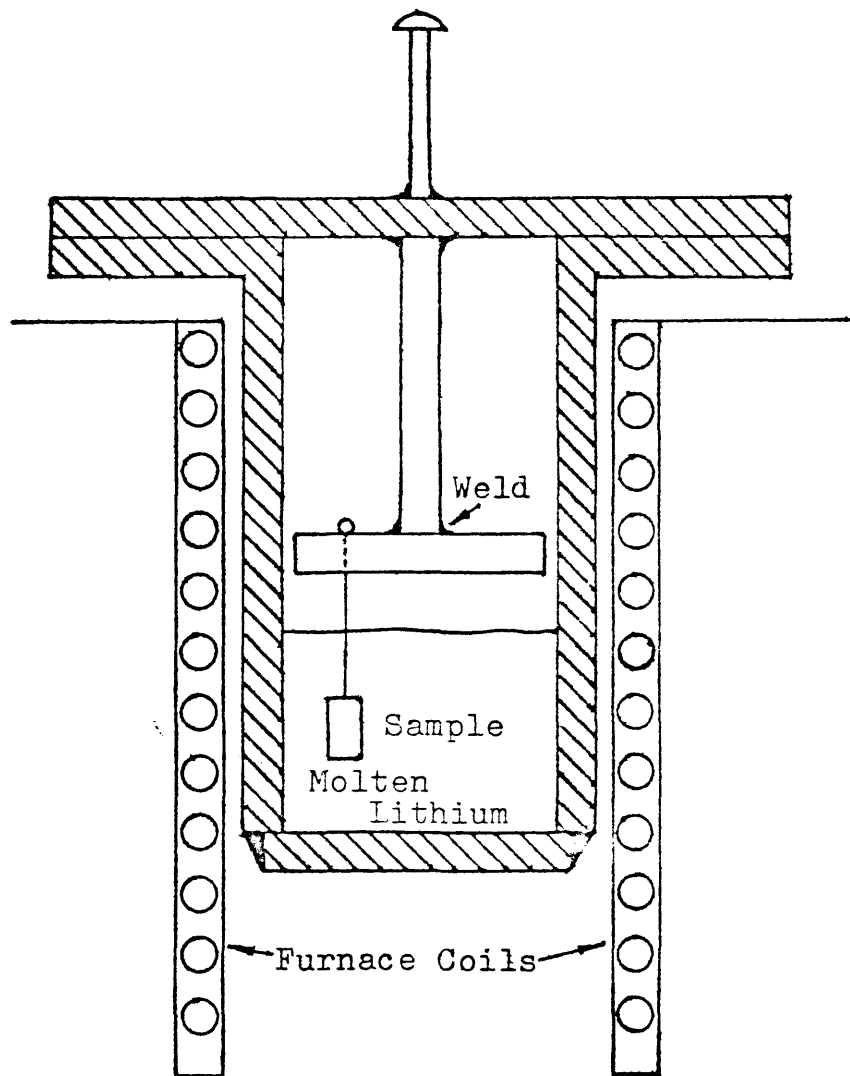


Figure 19. A schematic diagram of the test crucible and sample arrangement used in this investigation.

TABLE V. AN EXPERIMENTAL TEST MATRIX FOR TEMPERATURES AND TIMES

Temperature C	600	650	700	750	800	900
Penetration (max. time hrs.)	196	110	32	25	25	12
Weight loss (max. time hrs.)	196	110	32	25	169	12

Data generated by each of these tests is summarized in Appendix I

Testing

Two parameters were investigated, grain-boundary penetration, and weight loss. The test matrix used is given in table V.

Each sample, weighing about .5 grams, had the approximate dimensions .635 cm x 1.27 cm x .00762 cm. To assure that no dirt or oxide was present on any of the specimens, all samples were polished on #1 silicon carbide paper and then ultrasonically cleaned in methanol. The specimens were then weighed to ± 0.1 milligram. Afterwards, thickness measurements to ± 0.0001 inch were recorded.

The test was initiated by charging the crucible with 38 cubic centimeters of lithium. Before the rod was placed in the crucible it was wiped clean to remove surface compounds and mineral oil. The crucible was heated to test temperature and allowed to stabilize for 6 hours, thus removing any transient concentration gradients.⁽⁵²⁾ The 304-L stainless steel samples were placed in the crucible. During the test samples were periodically removed. After removal, the samples were cleaned completely in water, dissolving any adhering lithium, again in ultrasonic methanol. Following a final weighing, metallography was performed.

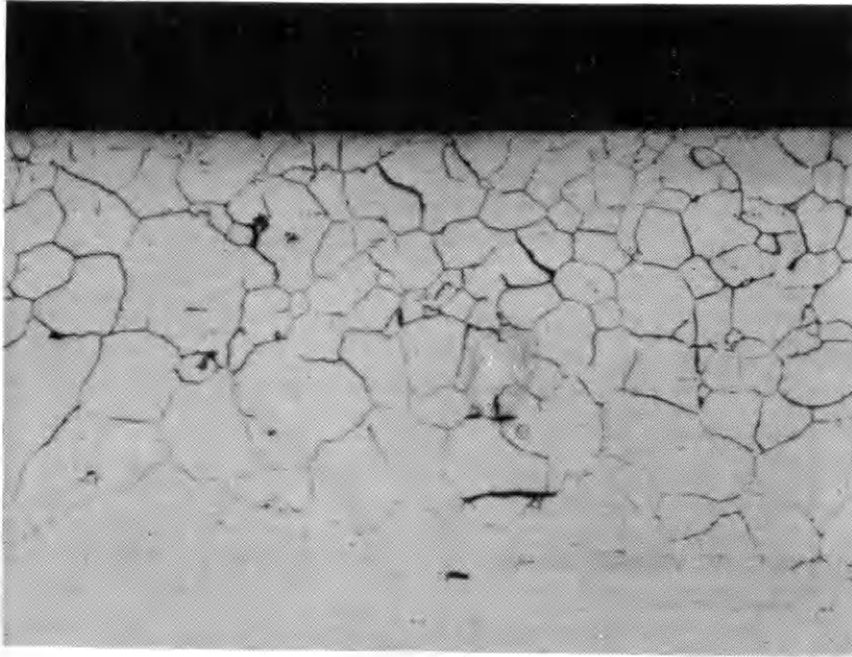
The penetration depth of lithium into the stainless steel was determined by optical metallography. Each sample, sandwiched between two protective metal strips, was mounted in Bakelite. The specimen was polished through a .05 micron alumina wheel and

etched by one of two equivalent mediums. Two etches were investigated to eliminate the possibility that the observed penetration was dependent on metallographic techniques. The etches and metallographic procedures are given in table VI. The same typical penetration pattern is revealed, figure 20, when the two etches are used, thus adding confidence to the metallographic procedures.

TABLE VI. A LISTING OF THE ETCHES AND METALLOGRAPHY PROCEDURES

<u>REAGENT</u>	<u>COMPOSITION</u>	<u>PROCEDURE</u>
FeCl_3 - HCl 1- used for most of the penetration study	FeCl_3 ----- 5 g. HCl ----- 50 ml H ₂ O ----- 100 ml	Etch for 60 seconds to reveal general structure plus penetration - follow by slight polish and etch for 20 seconds to reveal only the penetration.
Oxalic Acid	Oxalic Acid --- 10 g. H ₂ O ----- 100 ml	Used electrolytically with specimen as the anode. A current of .3 amps. for 2 minutes reveals the penetration very distinctly.

Ferric
chloride:



Oxalic
acid.....:

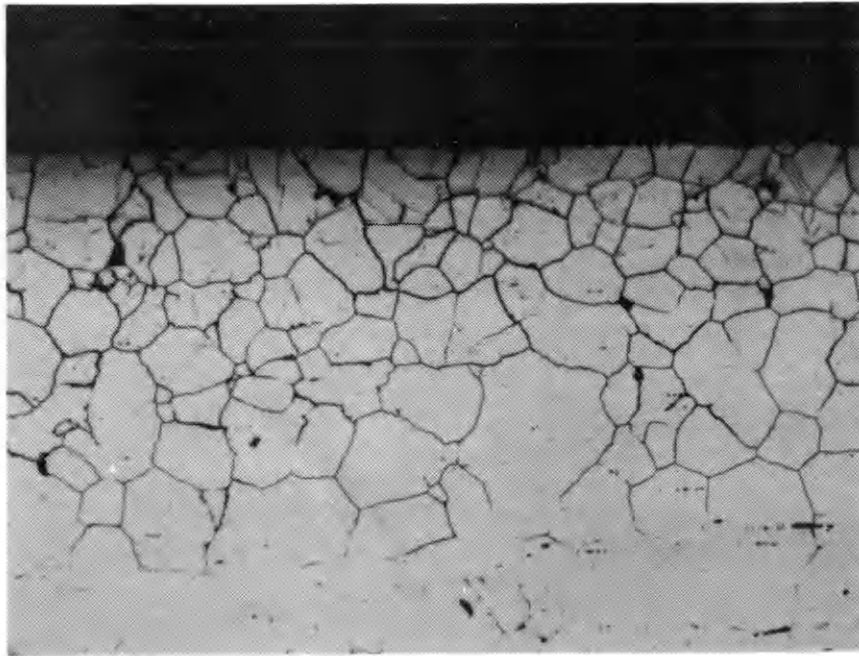


Figure 20. Photo-micrograph showing the penetration pattern as revealed by the two etches. X 200

DISCUSSION AND RESULTS

Two different modes of attack were found: (1) preferential grain-boundary penetration, and (2) surface deterioration or dissolution. The results describe a static-isothermal test in an all 304-L stainless steel-liquid lithium environment.

Grain-Boundary Penetration

If a penetrated sample was bent after it was exposed to lithium it cracked to the penetrated depth. (See figure 21.) It was also found, at the loss of a crucible, that penetrated 304-L is permeable to liquid lithium. Thus structural and impermeable integrity are lost by lithium penetration.

All penetration measurements were taken perpendicular to the edge of the nitrided sample, and represent a 10 reading average. To establish the present corrosion system was equivalent to the work of Patterson,⁽⁷¹⁾ his 800° C penetration test was duplicated. Figure 22 shows the two systems are the same for similar conditions.

Figures 23-28 show the penetration results, plotted as penetration depth versus $t^{1/2}$, for nitrided and as-received 304-L⁽⁷¹⁾ at 600° C, 650° C, 700° C, 750° C, 800° C, and 900° C. The rates are parabolic and empirically conform to



Figure 21. Bend test showing sample cracking after exposure to liquid lithium at 800° C, 9 hours. X 200

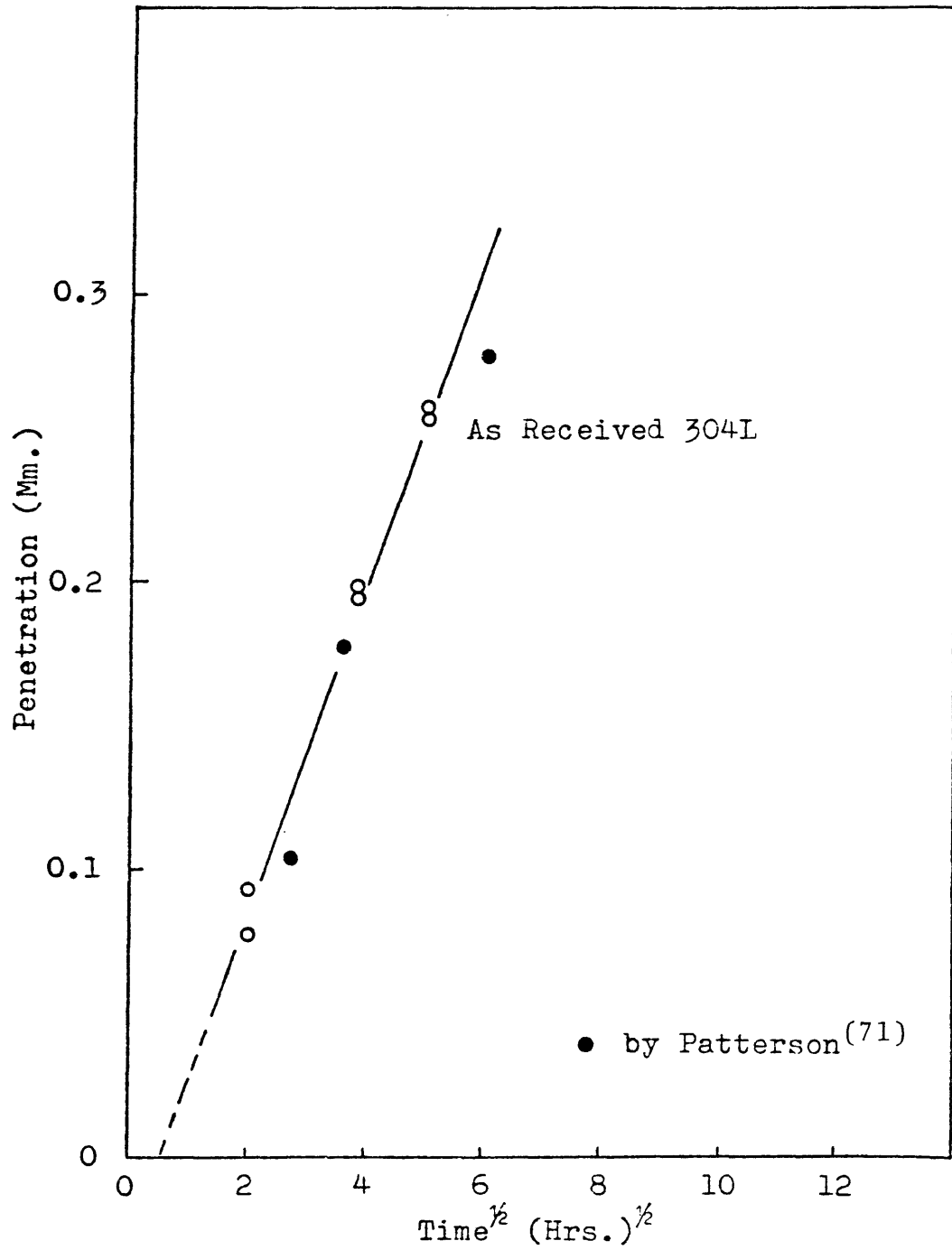


Figure 22. A graph of penetration depth versus the square root of time at 800° C for as-received 304-L stainless steel. (71)

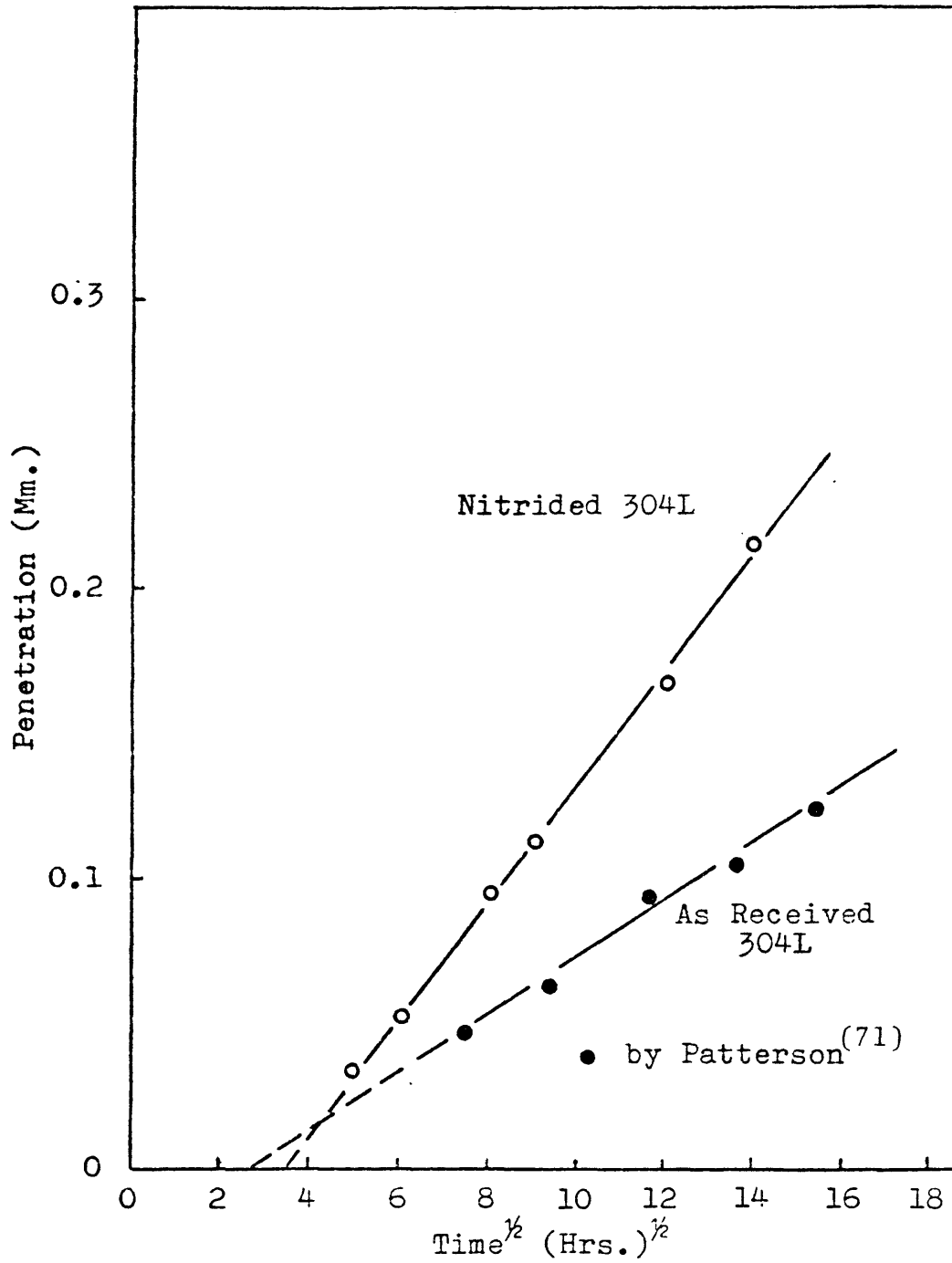


Figure 23. A graph of penetration depth versus the square root of time at 600° C for as-received⁽⁷¹⁾ and nitrided⁽⁷¹⁾ 304-L stainless steel.

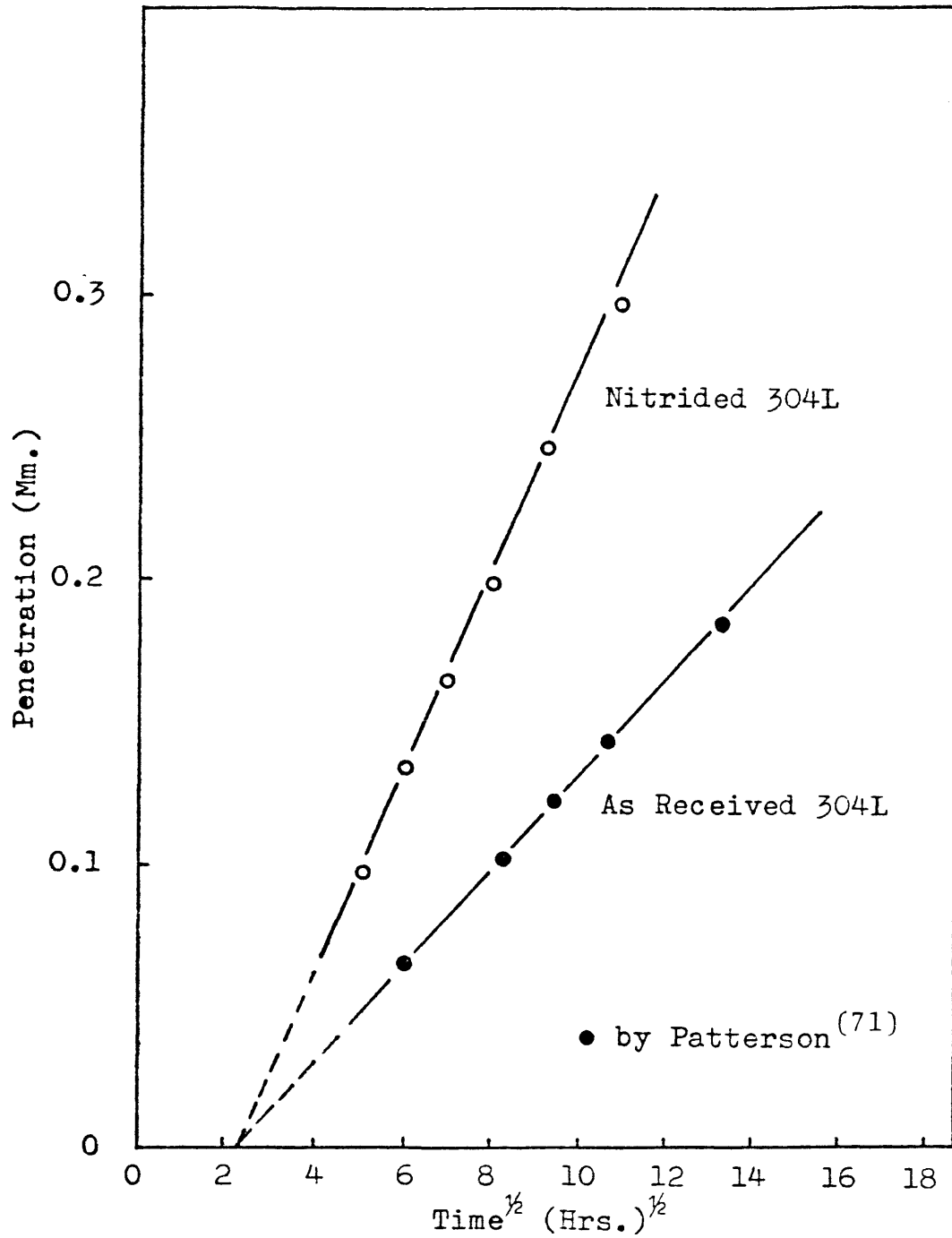


Figure 24. A graph of penetration depth versus the square root of time at 650° C for as-received⁽⁷¹⁾ and nitrided 304-L stainless steel.

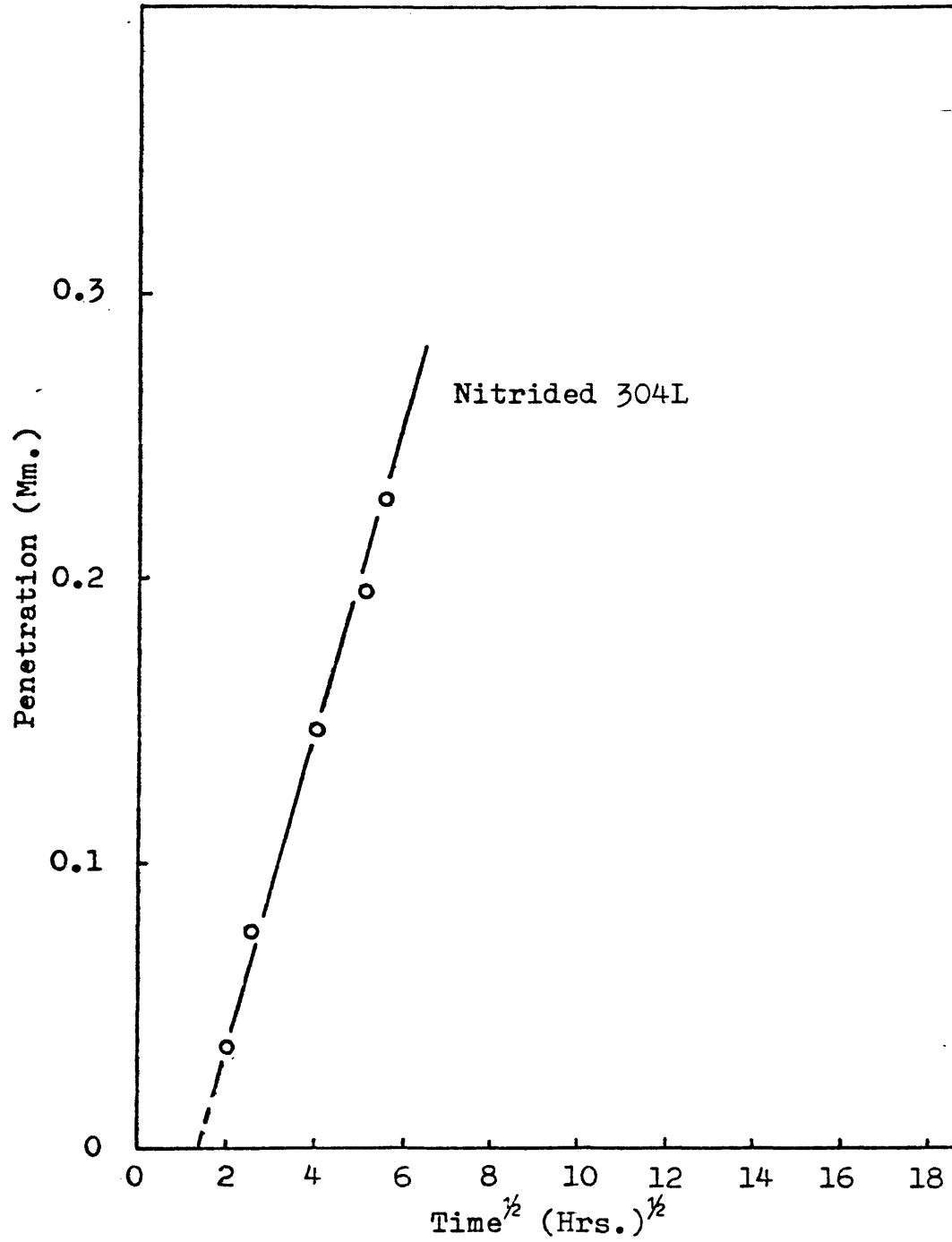


Figure 25. A graph of penetration depth versus the square root of time at 700° C for nitrided 304-L stainless steel.

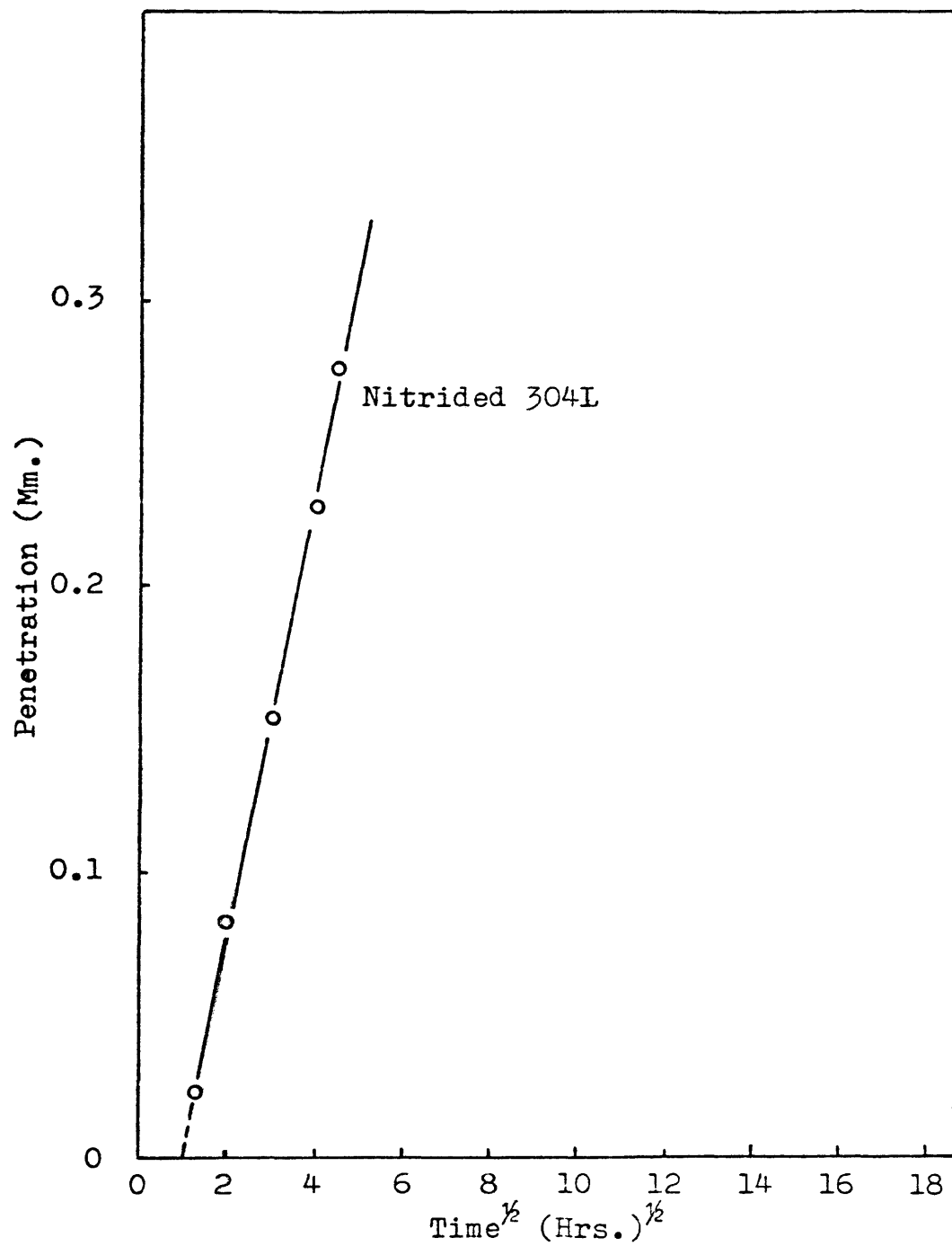


Figure 26. A graph of penetration depth versus the square root of time at 750° C for nitrided 304-L stainless steel.

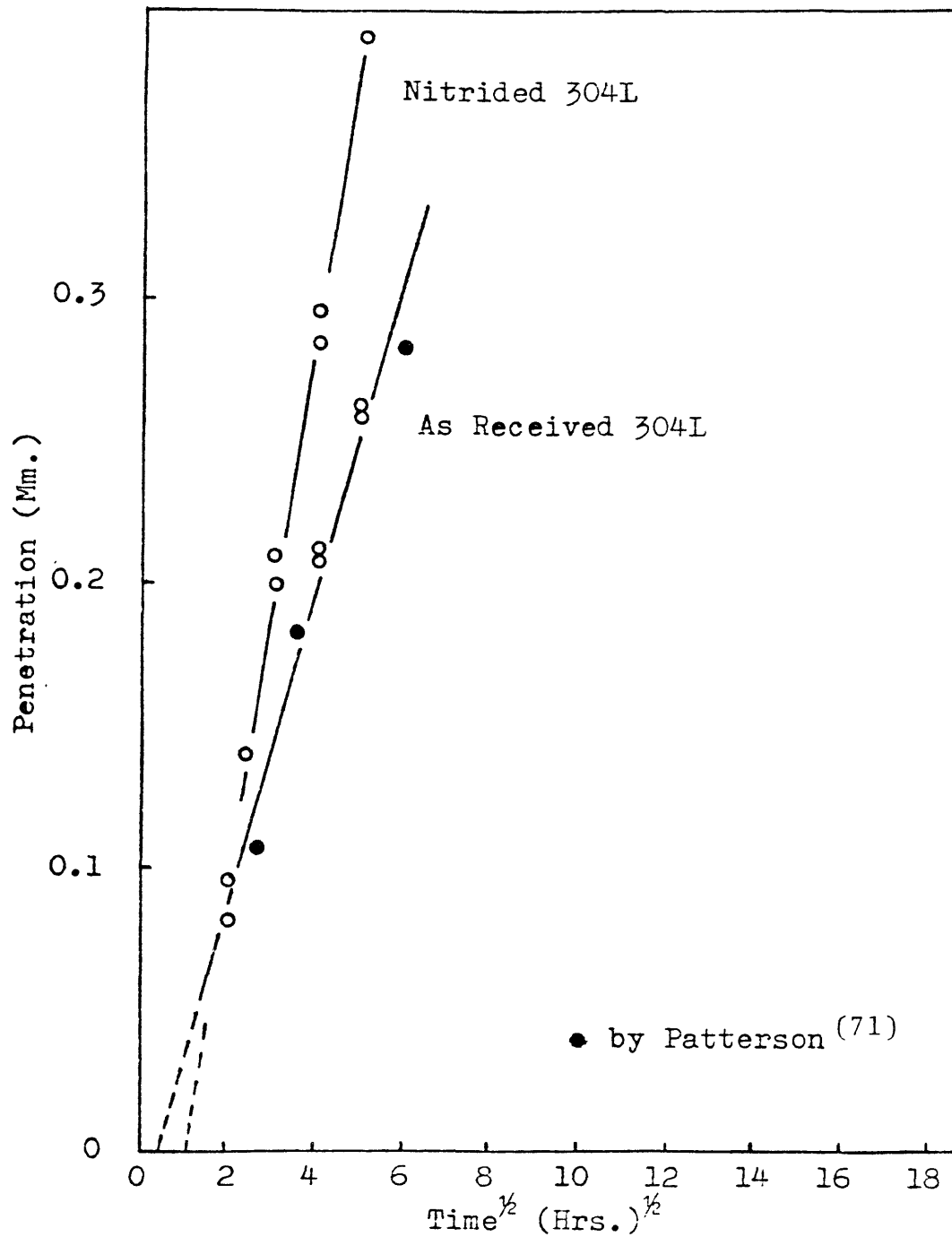


Figure 27. A graph of penetration depth versus the square root of time at 800° C for as-received (71) and nitrided 304-L stainless steel.

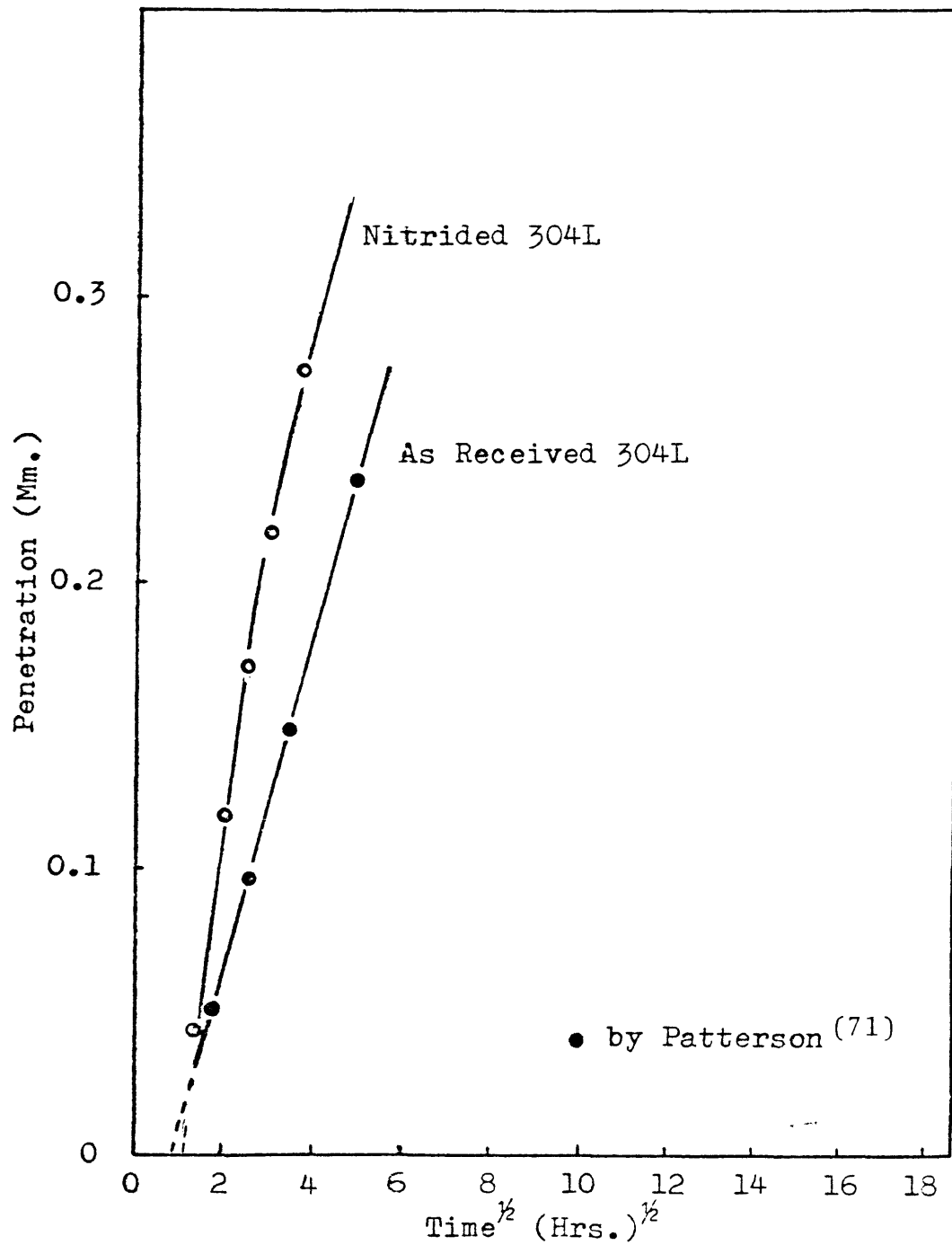


Figure 28. A graph of penetration depth versus the square root of time at 900° C for as-received⁽⁷¹⁾ and nitrided⁽⁷¹⁾ 304-L stainless steel.

$$x = \sqrt{Kt} \quad \text{eq. 29}$$

Figure 29, an Arrhenius plot, shows the temperature dependence of K is exponential

$$K = K_1 \exp\left(\frac{-Q_1}{RT}\right) \quad T > 747^\circ \text{ C} \quad \text{eq. 30}$$

$$K = K_2 \exp\left(\frac{-Q_2}{RT}\right) \quad T < 747^\circ \text{ C} \quad \text{eq. 31}$$

The two slopes shown indicate a change in processes has occurred.

Patterson,⁽⁷¹⁾ generalizing the previous model of Brehm, predicts

$$x = \sqrt{Kt} \quad \text{eq. 21}$$

$$\text{where } K_2 = 2D_2 \left[\left(\frac{C_S - C_1}{C_2 - C_1} \right) - \frac{1}{3} \left(\frac{C_S - C_2}{C_2 - C_1} \right)^2 + \dots \right] \quad \text{eq. 27}$$

The definitions of C_2 , C_1 , and C_S follow from figure 15. D_2 , the diffusion coefficient in the two-phase region, is

$$D_2 = D_0 \exp\left(\frac{-Q}{RT}\right) \quad \text{eq. 28}$$

In several corrosion systems, the corrosion product has a liquid solid transition temperature. For instance, the (Nb-O-Li) complex melts at 1100° C ^(45,79) and the lithium carbide product behaves in a similar fashion. ⁽⁷⁰⁾

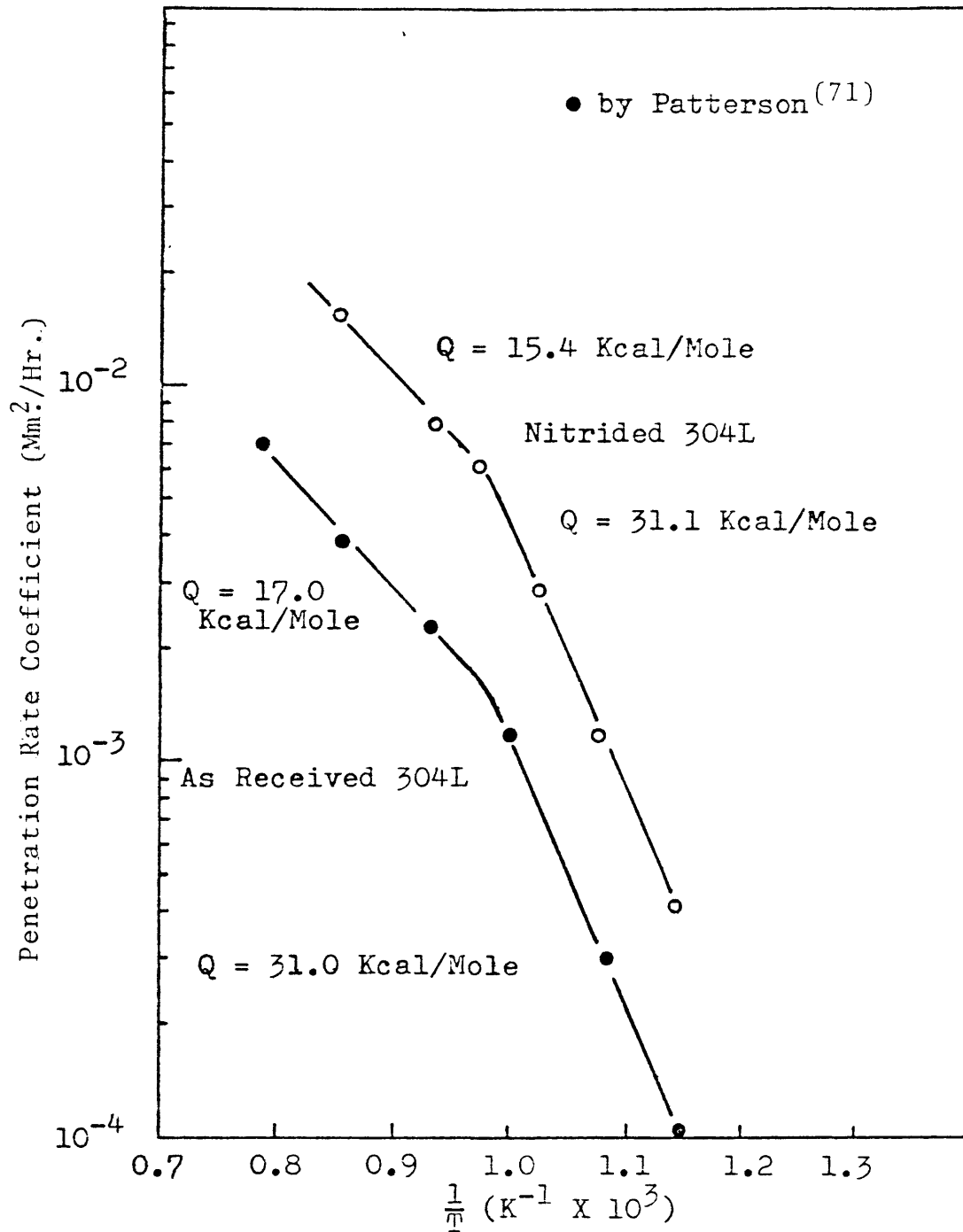


Figure 29. An Arrhenius plot showing the temperature dependence of grain-boundary penetration rate for as-received⁽⁷¹⁾ and nitrided 304-L stainless steel.

It is proposed that the same behavior is responsible for the activation change. Above 747°C a liquid phase, a (Li-Me-N) complex, exists at the grain boundaries while below 747°C a solid phase is present. Equating equations 27 and 30, $T > 747^{\circ}\text{C}$,

$$K_1 \exp\left(\frac{-Q_1}{RT}\right) = D_o \exp\left(\frac{-Q}{RT}\right) \left[2\left(\frac{C_S - C_1}{C_2 - C_1}\right) - \frac{2}{3}\left(\frac{C_S - C_2}{C_2 - C_1}\right)^2 \dots \right]$$

therefore $Q_1 = Q$ eq. 32

and
$$K_1 = D_o \left[2\left(\frac{C_S - C_1}{C_2 - C_1}\right) - \frac{2}{3}\left(\frac{C_S - C_2}{C_2 - C_1}\right)^2 \dots \right]$$
 eq. 33

Thus the lower activation energy in figure 26 represents lithium diffusion in a liquid phase, while K_1 is a function of D_o and various interfacial concentrations. Likewise, for $T < 747^{\circ}\text{C}$,

$$Q_2 = Q \quad \text{eq. 34}$$

and
$$K_2 = D_o \left[2\left(\frac{C_S - C_1}{C_2 - C_1}\right) - \frac{2}{3}\left(\frac{C_S - C_1}{C_2 - C_1}\right)^2 \dots \right]$$
 eq. 35

Q_2 is the activation energy for the diffusion of lithium in a solid (Li-Me-N) product. K_2 is again a function of D_o and interfacial concentrations.

The nonmechanistic increase in rate between the nitrated and as-received⁽⁷¹⁾ samples is related to a variation in D_o or interfacial concentrations.^(48,49) Brehm observed a similar increase as the oxygen impurities were increased in niobium. (See figure 9.) Likewise the interstitial impurities in pure

iron,⁽³⁶⁾ figure 8, increase D_0 for sodium and potassium diffusion, Assuming

$$D_0 = \nu a^2 \exp\left(\frac{-\Delta S}{R}\right) \quad \text{eq. 36}$$

where ν is the jump frequency, a is a crystallographic constant, and S is the entropy of mobility. Thus the increase in D_0 implies the jump frequency increased and/or the entropy decreased. Likewise an increase in K_2 can be caused by interfacial concentration changes.

Given in table VII are the rate constants for both the nitrated and as-received⁽⁷¹⁾ specimens. The subsequent activation energies are shown in table VIII. In figure 28 the nitrogen is diffusing out of the specimen causing the slope to decrease. This behavior is seen in both oxygen-doped niobium and nitrated 316 stainless steel lithium systems.

Inherent to figures 23-28 is a delay time. The observed delay is compared to the work of Patterson⁽⁷¹⁾ in figure 30. Also shown is the nucleation time for a $M_{23}C_6$ in 316-L stainless steel. The difference between the carbide nucleation and delay time suggest the delay is corrosion product nucleation. Initially as temperature increases, the delay time decreases, suggesting mass transport kinetics are controlling. If the corrosion product, as suggested,⁽⁴⁰⁾ is $Li_3N \cdot FeN$ the stability of this compound is decreasing as temperature increases. The Li_3N component is not stable (see figure 9) above 812° C.

TABLE VII. PENETRATION RATE CONSTANTS

<u>T (C)</u>	<u>T (K)</u>	<u>1/T (K⁻¹)</u>	<u>Rate Coefficient (Mm²/Hr.)</u>	
			<u>As Received⁽⁷¹⁾</u>	<u>Nitrided</u>
600	873	.001145	.00010	.00038
650	923	.001083	.000296	.00123
700	973	.001077	-	.00274
727	1000	.001000	.001176	-
750	1023	.000977	-	.00572
800	1073	.000932	.00228	.00829
900	1173	.000853	.00384	.01538
1000	1273	.000786	.00706	-

TABLE VIII. ACTIVATION ENERGIES

	<u>As Received⁽⁷¹⁾</u>	<u>Nitrided</u>
	<u>Kcal/Mole</u>	<u>Kcal/Mole</u>
Below 747 C -----	31.0	31.1
Above 747 C -----	17.0	15.4

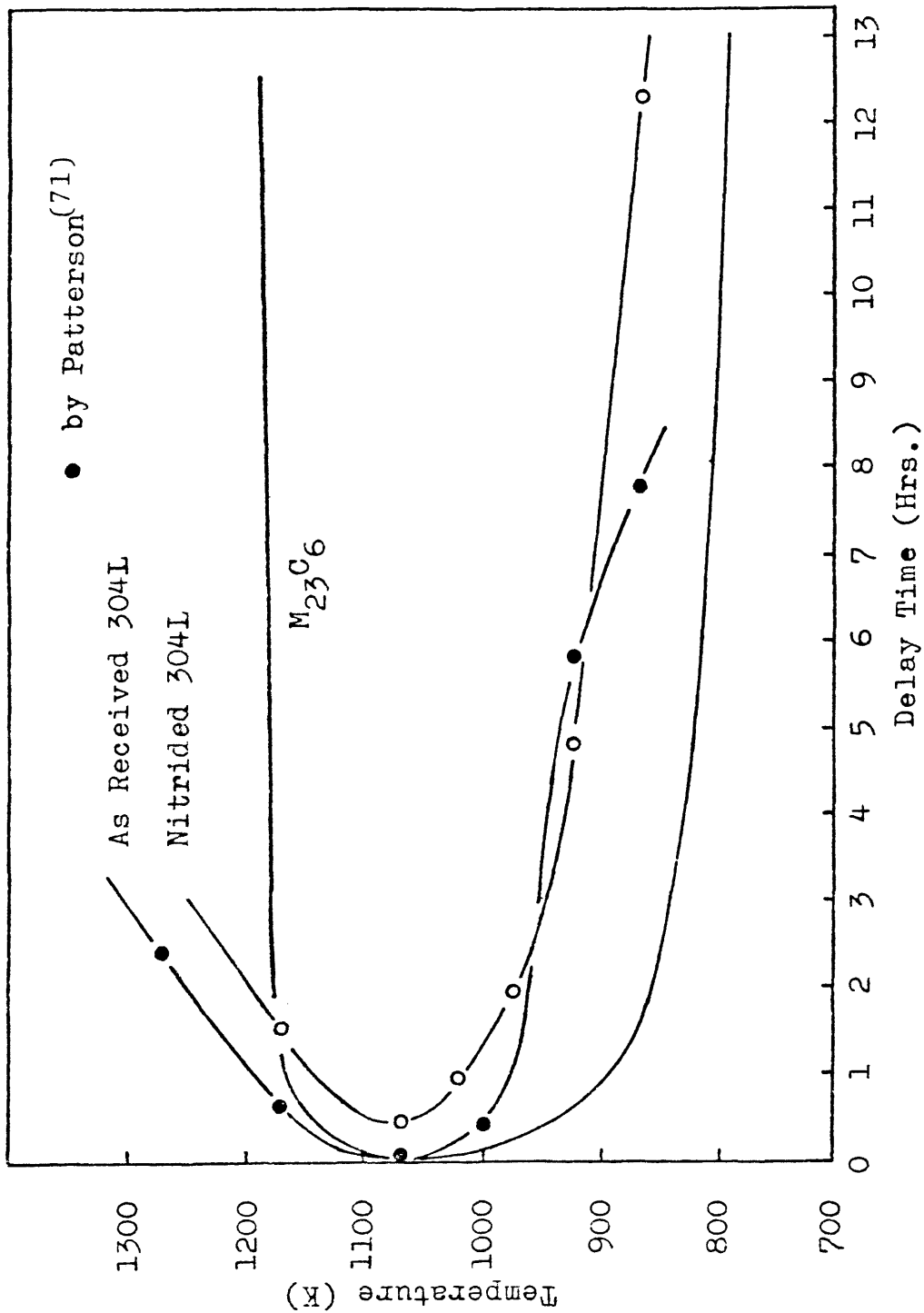


Figure 30. The time needed to nucleate a metal carbide in 316-L stainless steel (74) compared with the delay times in as-received (71) and nitrided 304-L stainless steel.

As the temperature increases above 812^o C, the nose of the delay curve, the corrosion product stability is decreasing and a longer incubation period is required.

Uniform Corrosion and Weight Loss

The weight loss, representing uniform corrosion and surface deterioration, was not investigated in detail. Measurements beyond the penetration times were not sought. As seen earlier, a penetrated sample loses structural and impermeable integrity. Thus penetration, and not weight loss, is the controlling design factor in any Li-304-L stainless steel system.

Figures 31-35 show weight loss measurements for as-received (71) and nitrided 304-L specimens. Dissolution attack begins immediately, indicating the delay time is not a wetting phenomenon. The weight loss empirically obeys a parabolic relationship

$$wt = \frac{\text{weight loss}}{\text{unit area}} = \sqrt{Kt} \quad \text{eq. 37}$$

However, the curves show a duplex behavior at longer times; thus another type of parabolic process is occurring.

The initial portion of each curve is a uniform corrosion attack. It obeys a parabolic relationship, (38,40) since it is controlled by the diffusion of specimen alloy constituents. However, this point is open to debate.

The increase in rate at later times represents surface deterioration. Transgranular penetration (see figure 36),

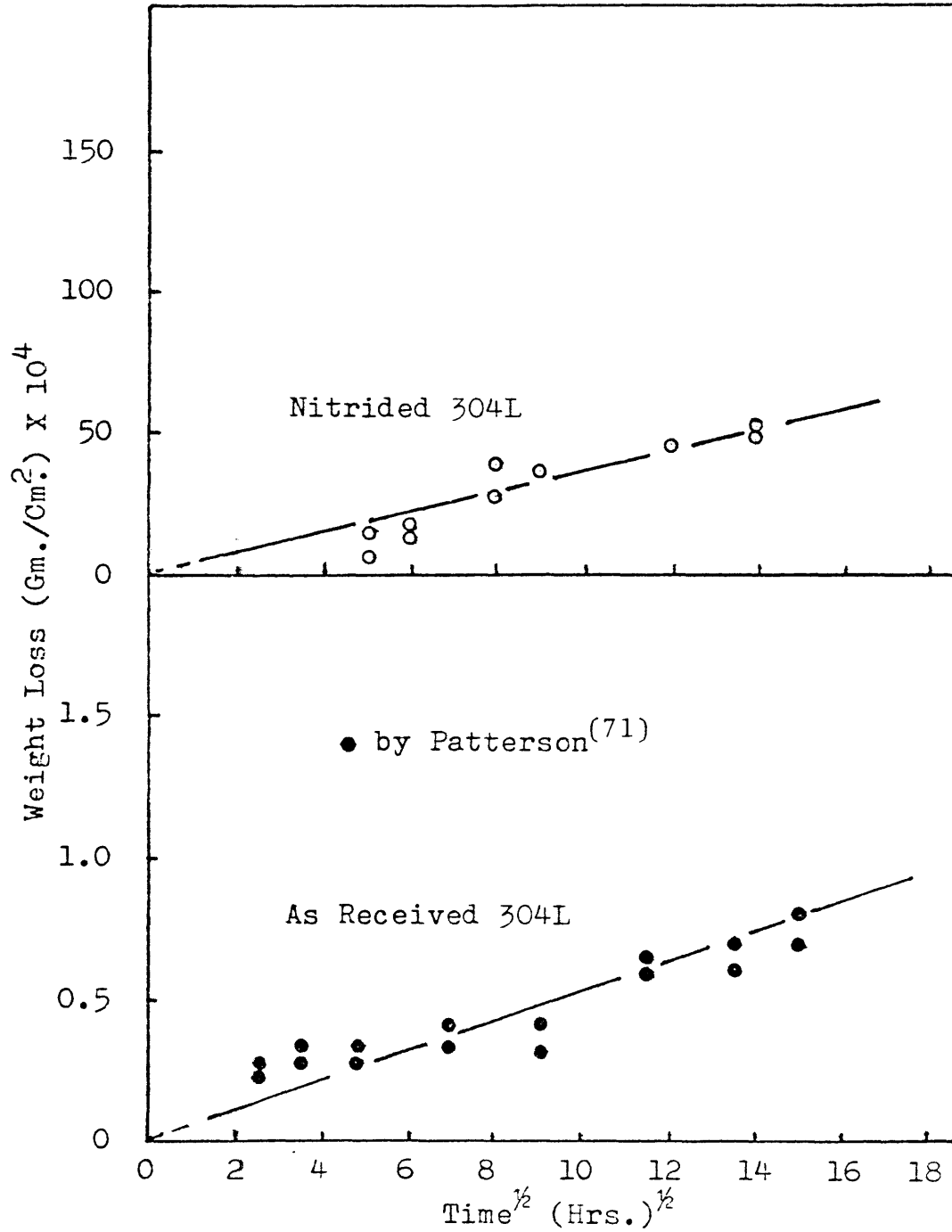


Figure 31. A graph of weight loss per unit surface area versus the square root of time at 600°C for as-received⁽⁷¹⁾ and nitrided 304-L stainless steel. (Note different weight loss scales.)

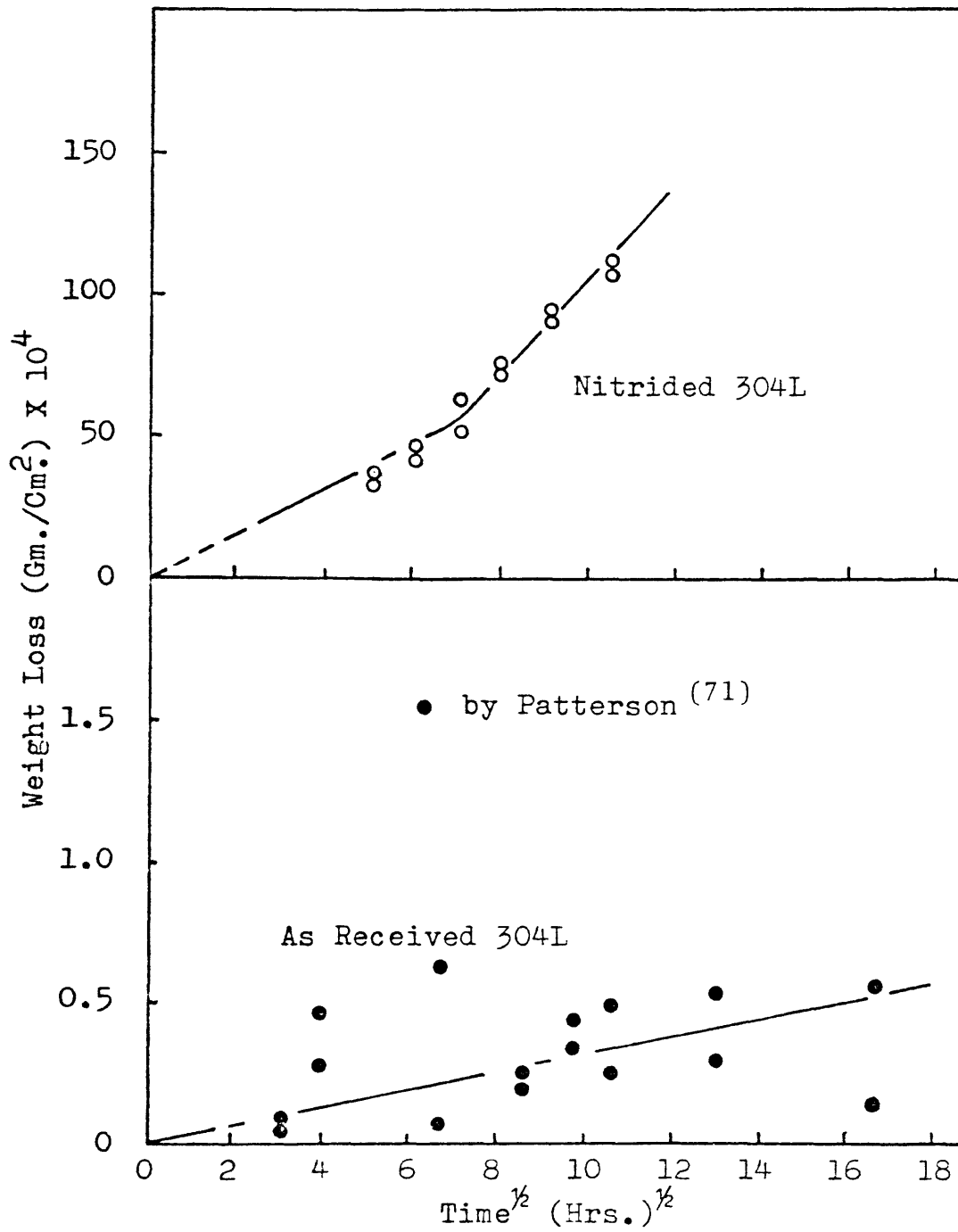


Figure 32. A graph of weight loss per unit surface area versus the square root of time at 650°C for as-received⁽⁷¹⁾ and nitrided 304-L stainless steel. (Note different weight loss scales.)

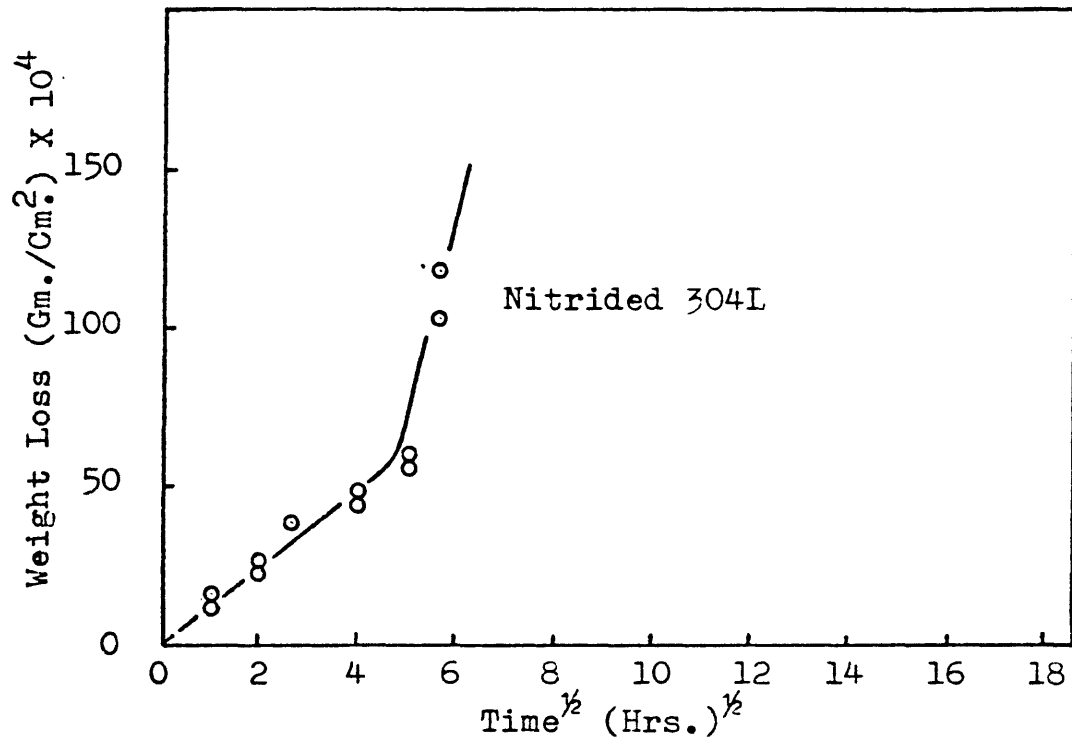


Figure 33. A graph of weight loss per unit surface area versus the square root of time at 700°C for nitrided 304-L stainless steel.

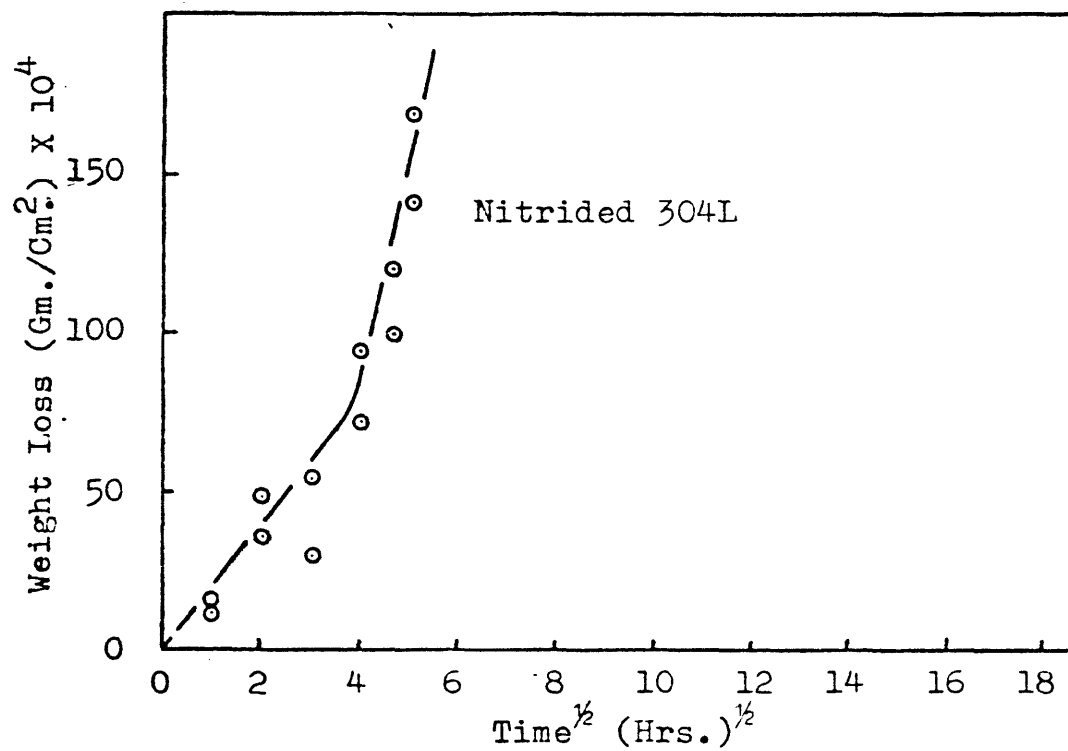


Figure 34. A graph of weight loss per unit surface area versus the square root of time at 750° C for nitrided 304-L stainless steel.

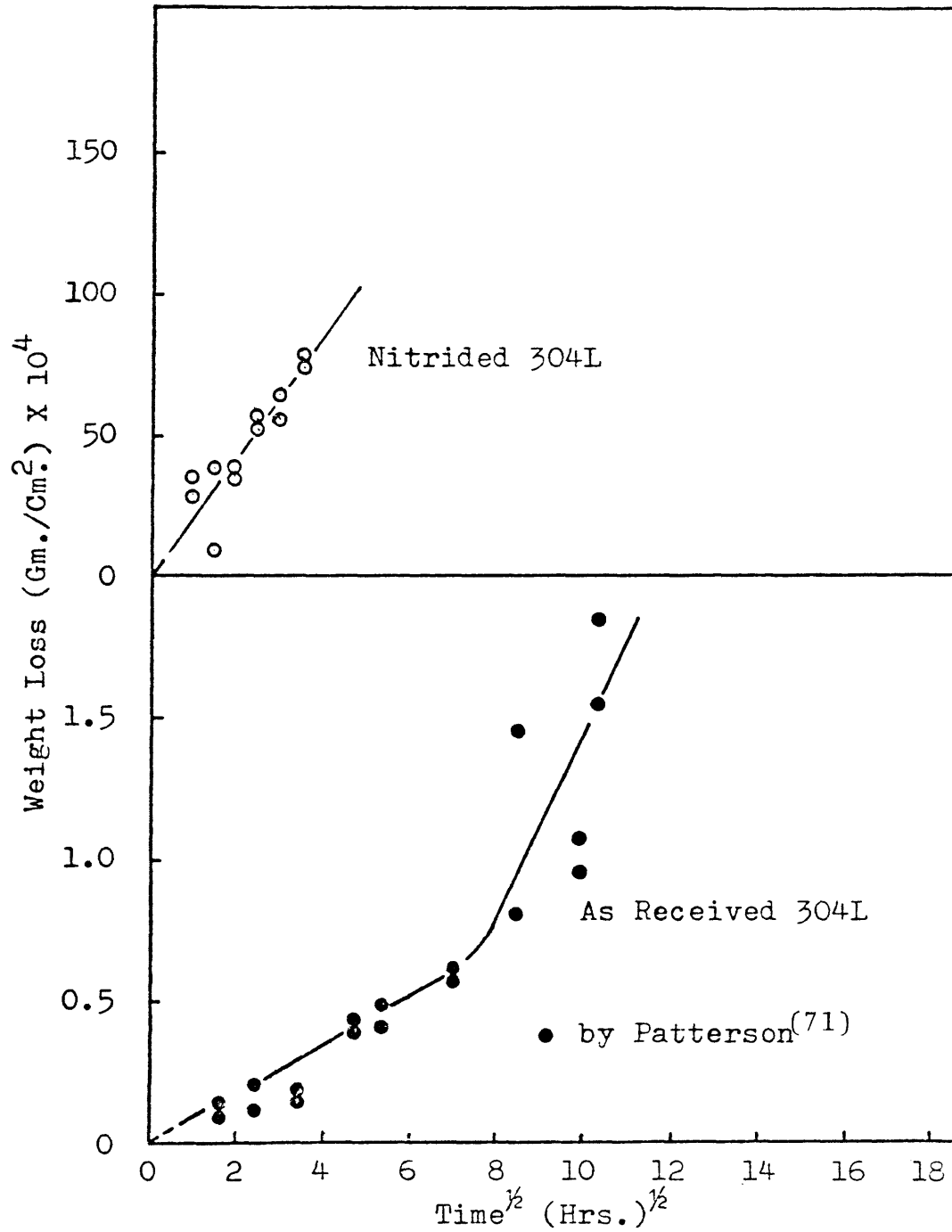


Figure 35. A graph of weight loss per unit surface area versus the square root of time at 900°C for as-received⁽⁷¹⁾ and nitrided 304-L stainless steel. (Note different weight loss scales.)

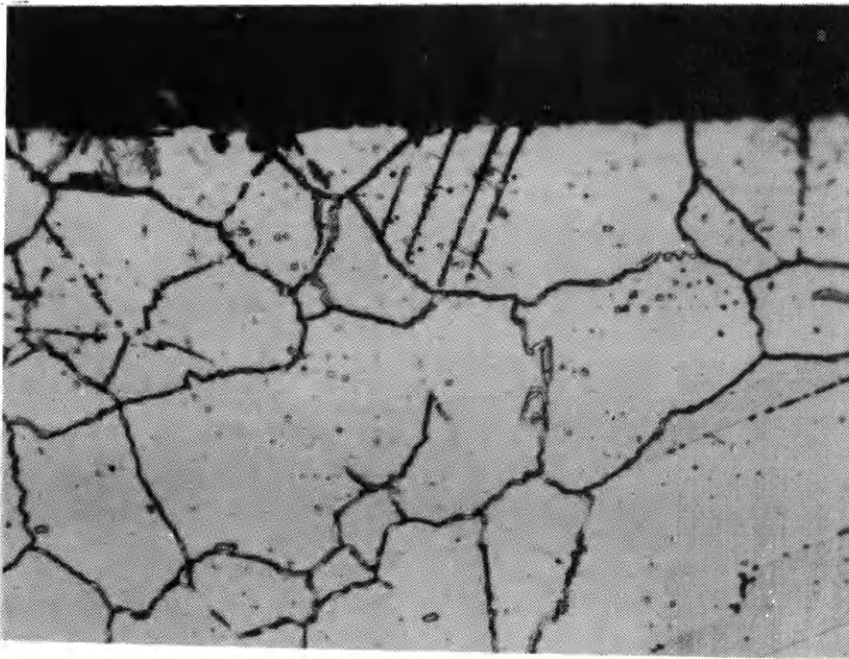


Figure 36. A photo-micrograph showing transgranular penetration of nitrided 304-L stainless steel by liquid lithium at 800° C, for 25 hours. X 500

seen in other alkali metal systems, (9,50,52,60,69) destroys the individual grains and eventually causes a breaking up and degradation of the surface. (See figure 37.) The result, diffusion-controlled transgranular penetration, is a highly localized attack, increasing weight loss.

An initial weight loss Arrhenius plot, figure 38, suggests a thermally controlled process below 747° C. The similar slope changes for weight loss and grain-boundary penetration, at 747° C imply the same mechanisms are responsible for the processes. A solid-liquid transition for the corrosion product explains weight loss activation. Below 747° C the solid corrosion product forms and remains at the surface. Thus the lithium must diffuse through the product, to the corrosion interface resulting in a parabolic weight loss rate. The activation energy for weight loss is in agreement with the activation energy for penetration. However, above 747° C the corrosion product is a liquid and does not remain at the specimen's surface. The lithium freely attacks and another mechanism, possibly alloy diffusion from the sample or chemical attack, controls. The values for the rate coefficients and activation energies are given in table IX.

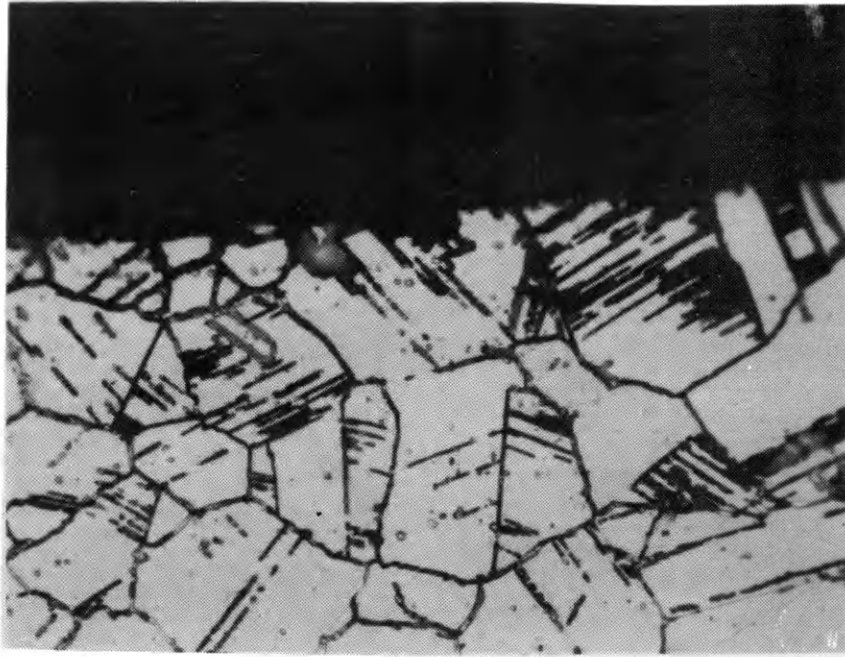


Figure 37. A photo-micrograph showing surface deterioration and degradation of nitrided 304-L stainless steel by liquid lithium at 800°C for 144 hours. X 500

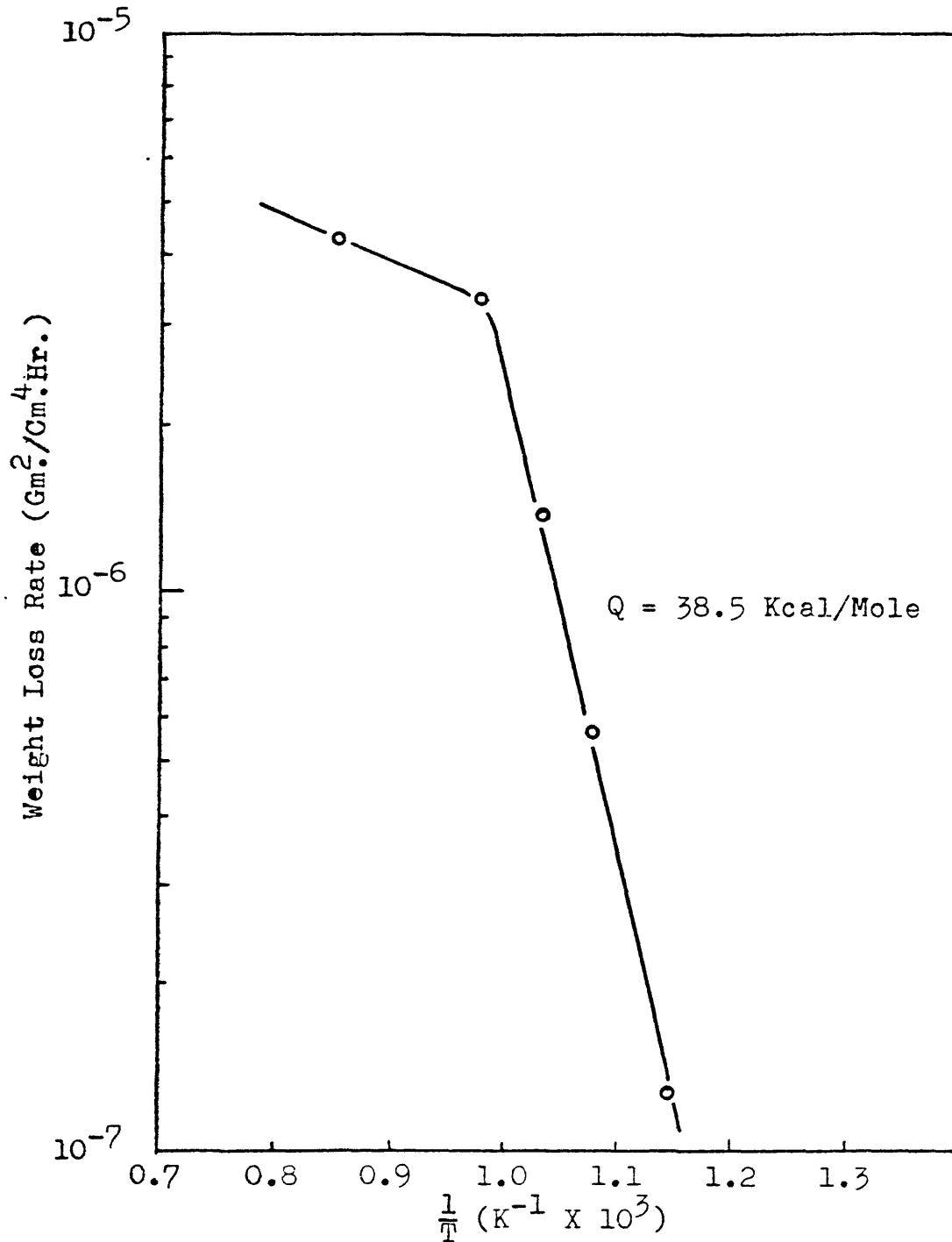


Figure 38. A graph showing the temperature dependence for the initial slope of the nitrided 304-L stainless steel weight loss curves.

TABLE IX. WEIGHT LOSS RATE COEFFICIENTS AND ACTIVATION ENERGY

<u>T (C)</u>	<u>T (K)</u>	<u>1/T (K⁻¹)</u>	<u>Rate Coefficient (Gm²/Cm⁴-Hr) X 10⁶</u>
600	873	.001145	.1273
650	923	.001083	.5867
700	973	.001027	1.3670
750	1023	.000978	3.3856
900	1173	.000852	4.2025

Activation Energy Below 747 C ----- 38.5 Kcal/Mole

CONCLUSIONS

The most important facts this investigation revealed are:

- (1) The presence of nitrogen in a 304-L specimen does not change the corrosion mechanism but it does increase the rate.
- (2) A delay time is observed before grain-boundary attack occurs. This delay is associated with the time needed to nucleate a corrosion product, a (Li-Me-N) complex.
- (3) Grain-boundary penetration was shown consistent with a parabolic rate-diffusion model.
- (4) The activation energy for penetration was shown representative of lithium diffusion in a solid corrosion product below 747^o C. Likewise the activation energy above 747^o C is representative of lithium diffusion in a liquid corrosion product.
- (5) The weight loss represents two types of continuous consecutive attack. First a uniform corrosion later superimposed with a surface deterioration.
- (6) The activation energy for weight loss was shown consistent with a liquid-solid transition for the uniform corrosion product. Below 747^o C the activation energy is representative of lithium diffusion in a solid corrosion complex.

SUGGESTIONS FOR FURTHER RESEARCH

The results of this investigation suggest areas for further research:

- (1) An investigation to isolate and identify the corrosion product and its physical properties
- (2) The need for a method to accurately measure and control oxygen, nitrogen, and carbon impurities in lithium
- (3) An investigation to illustrate the effects of oxygen doping in a 304-L system
- (4) A delay time investigation, discovering how to stop the corrosion product from nucleating giving rise to a 304-L alloy with excellent resistance.

APPENDIX IExperimental Data

The following data have been converted into the values plotted in this investigation.

Grain Boundary Penetration Data

	<u>Time (Hrs.)</u>	<u>Penetration Depth (Mm.)</u>
600° C	25	.035
	36	.053
	64	.095
	81	.115
	144	.168
	196	.213
650° C	25	.097
	36	.123
	49	.165
	64	.199
	84.5	.247
	110.5	.286
700° C	4	.035
	7	.076
	16	.147
	25	.196
	32	.228
800° C	4	.115
	9	.198
	9	.210
	16	.284
	16	.296
	25	.392

	<u>Time (Hrs.)</u>	<u>Penetration Depth (Mm.)</u>
900° C	2.25	.041
	4	.116
	6.25	.165
	9	.219
	12.25	.276

Weight Loss Data

	<u>Time (Hrs.)</u>	<u>Weight Loss (Gm./Cm²x10⁴)</u>
600° C	25	4.96
	25	16.01
	36	16.79
	36	13.94
	64	38.31
	64	28.64
	81	37.62
	144	46.12
	196	49.13
	196	52.09
650° C	25	34.70
	25	36.13
	36	41.16
	36	47.19
	49	51.23
	49	63.55
	64	73.18
	64	75.11
	84.5	91.46
	84.5	93.31
	110.5	110.01
110.5	106.54	
700° C	1	12.49
	1	15.88
	4	25.29
	4	24.93
	7	38.34
	16	42.22
	16	47.24
	25	54.39
	25	58.86
	32	102.44
	32	118.63

	<u>Time (Hrs.)</u>	<u>Weight Loss (Gm./Cm.² x 10⁴)</u>
750 ^o C	1	14.65
	1	13.96
	4	35.89
	4	47.29
	9	30.21
	9	53.88
	16	93.75
	16	93.84
	21	118.97
	21	98.84
	25	140.70
	25	167.76
	900 ^o C	1
1		29.01
2.25		8.75
2.25		36.75
4		37.35
4		36.65
6.25		51.99
6.25		55.62
9		55.63
9		64.30
12.25		73.63
12.25		77.30

REFERENCES

1. W. F. Brehm, et al., "Radioactive Transport in Flowing Sodium Systems", Corrosion by Liquid Metals, Plenum Press, New York, (1970), Pp. 97-114.
2. J. R. DiStefano, and A. P. Litman, "Effects of Impurities in Some Refractory Metal--Alkali Metal Systems", 20th Annual Conference of the National Association of Corrosion Engineers, March 13, 1964.
3. G. A. Whitlow, et al., "Sodium Corrosion Behavior of Alloys for Fast Reactor Applications", Chemical Aspects of Corrosion and Mass Transfer in Liquid Sodium, AIME, (1971), Pp. 1-64.
4. E. Berkey and G. A. Whitlow, "Microstructural and Compositional Changes in Sodium-Exposed Stainless Steel by Scanning Electron Microscopy", Chemical Aspects of Corrosion and Mass Transfer in Liquid Sodium, AIME, (1971), Pp. 65-100.
5. K. T. Claxton and J. G. Collier, "Mass Transport of Stainless Steel Corrosion Products in Flowing Sodium", Chemical Aspects of Corrosion and Mass Transfer in Liquid Sodium, AIME, (1971), Pp. 101-129.
6. J. E. Eberhart, et al., "The Grain Boundary Grooving of Iron in Sodium", Corrosion by Liquid Metals, Plenum Press, New York, (1970), Pp. 461-467.
7. K. Natesan and T. F. Kassner, "Thermodynamics of Carbon Transfer in Sodium Steel Systems", Chemical Aspects of Corrosion and Mass Transfer in Liquid Sodium, AIME, (1971), Pp. 130-156.
8. S. A. Shields, et al., "Interstitial Mass Transfer in Sodium Systems", Chemical Aspects of Corrosion and Mass Transfer in Liquid Sodium, AIME, (1971), Pp. 157-176.
9. R. W. Harrison, "Corrosion of Oxygen Contaminated Tantalum in NaK", Corrosion by Liquid Metals, Plenum Press, New York, (1970), Pp. 151-176.
10. R. H. Hiltz, "The Corrosion of Stainless Steel in Oxygen Contaminated Sodium at 1200° F and 1400° F", Corrosion by Liquid Metals, Plenum Press, New York, (1970), Pp. 63-80.

11. K. Goldman, et al., "Some Fundamental Aspects of Carburization and Decarburization of Chromium Steels in Sodium Systems", Chemical Aspects of Corrosion and Mass Transfer in Liquid Sodium, AIME, (1971), Pp. 177-198.
12. E. D. Grosser, "Interstitial Element Movement in Potential Fuel Cladding Materials in Sodium", Chemical Aspects of Corrosion and Mass Transfer in Liquid Sodium, AIME, (1971), Pp. 199-206.
13. J. R. Weeks and H. S. Isaacs, "A General Model for Corrosion of Steels in High Velocity Sodium", Chemical Aspects of Corrosion and Mass Transfer in Liquid Sodium, AIME, (1971), Pp. 207-222.
14. E. E. Hoffman and W. D. Manly, "Corrosion Resistance of Metals and Alloys to Sodium and Lithium", Symposium on Handling and Uses of Alkali Metals, American Chemical Society, (1957), Pp. 82-91.
15. A. J. Romano, et al., "A Model for the Downstream Effects in the Corrosion of Steels by Liquid Sodium", Chemical Aspects of Corrosion and Mass Transfer in Liquid Sodium, AIME, (1971), Pp. 223-231.
16. S. J. Wachtel, et al., "A Role of Particulates in the Corrosion of Steels by Liquid Sodium", Chemical Aspects of Corrosion and Mass Transfer in Liquid Sodium, AIME, (1971), Pp. 232-240.
17. J. Hopenfeld, "Corrosion of Type 316 Stainless Steel With Surface Heat Flux in 1200^o F Flowing Sodium", Corrosion by Liquid Metals, Plenum Press, New York, (1970), Pp. 33-40.
18. G. W. Horsley, "Corrosion of Iron by Oxygen Contaminated Sodium", Journal of the Iron and Steel Institute, (1956), Pp. 43-48.
19. L. H. Kirschler, "A Limited Comparison of the Mechanical Strength of Austenitic Steel in 1200^o F, Sodium, Air and Helium", Journal of Basic Engineering, (Dec. 1969), Pp. 785-791.
20. J. E. Draley, "Some Consequences of the Maintenance of Equilibrium of Alloy Constituents Between the Surface of Stainless Steel and Sodium in a Recirculating System", Chemical Aspects of Corrosion and Mass Transfer in Liquid Sodium, AIME, (1971), Pp. 241-252.

21. B. A. Nevzorov, et al., "Controlling Stage in The Transfer of Carbon in the System Carbon Steel/Liquid Sodium/Cr-Ni Steel", Fiziko-Khimicheskaya Mekhanika Materialov, V. 3, No. 3, (1967), Pp. 257-260.
22. G. H. Rolster and A. J. Bogers, "An Expression for Mono-metallic Corrosion Rate in Liquid Sodium", Chemical Aspects of Corrosion and Mass Transfer in Liquid Sodium, AIME, (1971), Pp. 253-264.
23. H. V. Borgstedt and G. Frees, "Relations Between Corrosion Test Results and a Possible Mechanism of Liquid Sodium Corrosion", Chemical Aspects of Corrosion and Mass Transfer in Liquid Sodium, AIME, (1971), Pp. 265-277.
24. J. Sannier, et al., "Corrosion Behavior of Ferritic Steels in Flowing Sodium", Chemical Aspects of Corrosion and Mass Transfer in Liquid Sodium, AIME, (1971), Pp. 278-298.
25. A. J. Romano, et al., "Interaction Effects Between Dissimilar Metals in High Velocity Sodium at Temperatures Up to 760^o C", Corrosion by Liquid Metals, Plenum Press, New York, (1970), Pp. 21-32.
26. P. Roy, et al., "The Evaluation of Particulates Deposited in Flowing Non-Isothermal Sodium Systems", Liquid Metal Corrosion, Plenum Press, New York, (1970), Pp. 1-20.
27. P. A. Bague, et al., "Compositional Changes in Austenitic Steels after Corrosion in Sodium at 700^o C", Chemical Aspects of Corrosion and Mass Transfer in Liquid Sodium, AIME, (1971), Pp. 299-316.
28. B. Minushkin and G. Kissel, et al., "Hydrogen-Oxygen Interactions in Liquid Sodium", Chemical Aspects of Corrosion and Mass Transfer in Liquid Sodium, AIME, (1971), Pp. 317-332.
29. W. E. Ruther, et al., "Evaluation of Materials--Compatibility Problems in the EBR-II Reactor", Liquid Metal Corrosion, Plenum Press, New York, (1970), Pp. 81-96.
30. S. L. Schrock, et al., "Sodium Corrosion of Westinghouse Liquid Metal Fast Breeder Reactor Materials", Liquid Metal Corrosion, Plenum Press, New York, (1970), Pp. 41-62.

31. A. A. Smith, "Some Observations on the Interaction of Liquid Sodium with Cast Irons and Plain Carbon Steels", *Journal of the Iron and Steel Institute*, (Sept. 1960), Pp. 29-42.
32. M. G. Barker and D. J. Wood, "The Chemical Composition of Corrosion Products in Liquid Sodium", *Chemical Aspects of Corrosion and Mass Transfer in Liquid Sodium*, AIME, (1971), Pp. 365-380.
33. B. Berlin, "An Experimental Study of Mass Transfer and Alloying Behavior of Metals in Liquid Sodium", *Chemical Aspects of Corrosion and Mass Transfer in Liquid Sodium*, AIME, (1971), Pp. 403-419.
34. D. L. Smith and T. F. Kassner, "Application of Thermodynamics and Kinetic Parameters of the V-O-Na System to the Sodium Corrosion of Vanadium-Base Alloys", *Liquid Metal Corrosion*, Plenum Press, New York, (1970), Pp. 115-136.
35. R. B. Snyder, "Kinetics of the Carburization Process of Austenitic Stainless Steels in Sodium", *Journal of Nuclear Materials*, (1974), Pp. 259-274.
36. A. V. Tomulov, *et al.*, "A Study of Diffusion of Sodium and Potassium in Iron", *Fiziko-Khimicheskaya Mekhanika Materialov*, V. 3, No. 3, Pp. 261-263.
37. J. R. Weeks and H. S. Isaacs, "Corrosion and Deposition of Steels and Nickel Base Alloys in Liquid Sodium", *Advances in Corrosion Science and Technology*, V. 3, Plenum Press, (1973).
38. J. R. Weeks and C. J. Klamut, "Liquid Metal Corrosion Mechanisms", *Corrosion of Reactor Materials*, V. 27, No. 1, Vienna, (1962).
39. Lithium Corporation of America, "Lithium Metal as a Heat Transfer Medium", *LICOA Product Bulletin*, New York.
40. E. E. Hoffman, "Corrosion of Metals by Lithium at Elevated Temperatures", ORNL 2924.
41. E. M. Flenn, "Physical Properties of Lithium", *Lithium Corporation of America*, New York.
42. Chemical Rubber Company, "Handbook of Chemistry and Physics", *Chemical Rubber Company*, Ohio, 1969.

43. N. E. Holden and W. F. Walker, "Chart of Nuclides", Educational Relations, General Electric Co., N. Y., 12345, (Oct., 1972).
44. W. H. Sullivan, "Trilinear Chart of Nuclides", Oak Ridge National Laboratories, U. S. Government Office, Washington, D.C., (Jan. 1957).
45. W. D. Wilkinson, and W. F. Murphy, Nuclear Reactor Metallurgy, D. Van Nostrand Co., (1958), Pp. 263-288.
46. USAEC, "Major Activities in Atomic Energy Program", Jan-Dec 1959, U. S. Gov't. Printing Office, (1960).
47. R. N. Lyon, Liquid Metals Handbook 2nd Edition, USAEC and Department of the Navy, Report NAVEXOS-p. 73 (1952).
48. W. F. Brehm Jr., "Grain Boundary Penetration of Niobium by Lithium", PhD Thesis, NYO-3228-11, Report #735, Cornell University (1967).
49. W. F. Brehm, et al., "Grain Boundary Penetration of Niobium (Columbium) by Lithium", Transactions of the Metallurgical Society of AIME, V 242, (July 1968).
50. R. L. Klueh, "Penetration of Refractory Metals by Alkali Metals", Corrosion by Liquid Metals, Plenum Press, New York, (1970), Pp. 177-196.
51. J. R. DiStefano and E. E. Hoffman, "Relation Between O₂ Distribution and Corrosion of Refractory Metals in Lithium", Corrosion of Reactor Materials, V. 2, Vienna, (1962).
52. H. W. Leavenworth and R. L. Cleary, ACTA Metallurgica, V. 9, (1961), P. 519.
53. R. E. Cleary, et al., "Solubilities of Refractory Metals in Li and K", Pratt and Whitney Aircraft, (CANEL), Rept. TIM-850, (1965).
54. M. Kolodney and B. Minushkin, "A Method for Determining the Solution Rate of Container Metals in Li", Rept. NDA-41, (June 1957).
55. J. J. Sand and C. S. Grove, "Solubility of Fe in Liquid Li", Rept. OMCC-HEF-166, (Aug. 1958).

56. Y. F. Bychkov, et al., "Determining Solubility of Metals in Lithium", Metallurgy and Metallography of Pure Metals, No. 2, Moscow (1966).
57. A. S. Brasunas, "Liquid Metal Corrosion", Corrosion, V. 9, March, 1953, Pp. 78-84.
58. A. B. Johnson, Jr. and W. F. Vogelsang, "An Assessment of Corrosion Product Transfer Problem in a CTR", Transactions American Nuclear Society, V. 17, (Nov., 1973), P. 150.
59. D. Anthrop, "Solubilities of Transition Metals in Liquid Alkali and Alkaline Earth Metals, Lanthanum and Cerium; A Critical Review of Literature", Lawrence Radiation Laboratory, Livermore, Rept. UCRL-50315 (1968).
60. R. L. Klueh, "Oxygen Effects on the Corrosion of Niobium and Tantalum by Liquid Lithium", Metallurgical Transactions, V. 5, (April, 1974), Pp. 875-879.
61. D. L. Slatter and D. D. Howat, "Mass Transfer Effects in a Stainless Steel-Liquid Lithium-Uranium Carbide System", Journal of the Iron and Steel Institute, (Mar. 1970), Pp. 282-288.
62. W. D. Wilkinson, "Attack of Metals by Lithium", Argonne National Laboratory, Contract W-31-109-ENY-38, (1950).
63. M. S. Goikhman and M. I. Chaevskii, "Corrosion Resistance of Alloy EI-437B in Lithium", Fiziko-Khimicheskaya Mekhanika Materialov, V. 6, No. 5, (1970), Pp. 106-108.
64. Lithium Corporation of America, "Lithium Metal", LITHCOA Products Bulletin, New York.
65. Lithium Corporation of America, "Binary Phase Diagrams of Lithium", LITHCOA Products Bulletin, New York.
66. E. G. Brush, "Evaluation of Materials in Lithium (Corrosion Resistance of Ferritic and Austenitic Steels in Lithium at 500^o C)", General Electric, REPT #26, (1959)
67. M. S. Goikhman, et al., "Corrosion Failure of IKh18N9T 1Cc 18N9Ti Steel in Liquid Lithium", Fiziko-Khimicheskaya Mekhanika Materialov, V. 4, No. 6, (1968), Pp 671-675.
68. R. W. Harrison, "The Effects of Welding Atmosphere Purity on the Lithium Corrosion Resistance of Refractory Alloys", Corrosion by Liquid Metals, Plenum Press, New York, (1970), Pp. 151-176.

69. W. M. Phillips, "Some Alkali Metal Corrosion Effects in a Rankine Cycle Test Loop", Corrosion by Liquid Metals, Plenum Press, New York, (1970), Pp. 197-216.
70. V. V. Popovich, et al., "Corrosion Resistance of Armco Iron in Liquid Lithium", Fiziko-Khimicheskaya Mekhanika Materialov, V. 31, No. 1, (1967), Pp. 23-32.
71. R. A. Patterson. "Liquid Lithium Corrosion of 304-L Stainless Steel", M.S. Thesis, Colorado School of Mines, T-1684, (1974).
72. G. G. Maksimovich, et al., "Changes in the Fine Structure of 1Cr18Ni9Ti Steel After Protracted Loading in Lithium", Fiziko-Khimicheskaya Mekhanika Materialov, V. 6, No. 3, (1970).
73. J. M. McKee, "Effect of Nitrogen on Corrosion by Lithium), Rept. NDA-40, (June 1957).
74. B. Weiss and R. Strickler, "Phase Instabilities During High Temperature Exposure of 316 Austenitic Stainless Steel", Met. Trans., V. 3, (April 1972), Pp. 851-865.
75. E. M. Simons, "IAEA Symposium on Alkali-Metal Coolants", Reactor Materials, V. 10, No. 2, (1967), Pp. 96-103.
76. E. M. Simons, "Corrosion by Nonaqueous Liquids and Vapors", Reactor Materials, V. 12, No. 2, (1969), Pp. 98-103.
77. E. M. Simons, "Corrosion by Nonaqueous Liquids and Vapors", Reactor Materials, V. 13, No. 1, (1970), Pp. 97-101.
78. E. M. Simons, "Corrosion by Nonaqueous Liquids and Vapors", Reactor Materials, V. 13, No. 3, (1970), P. 149.
79. A. Riesman, J. Am. Chem. Soc., 6503, (1958).
80. E. E. Hoffman, "Liquid Metal Corrosion", Corrosion Fundamentals, University of Tennessee Press, (1956), P. 78.
81. G. H. Whitlow, et al., "The Effects of Exposure to Flowing Sodium on Vanadium Alloys in Stainless Steel Containment Systems", Corrosion by Liquid Metals, Plenum Press, New York, (1970), Pp. 115-136.
82. L. E. Kindlimann and G. S. Ansell, "Kinetics of the Internal Nitridation of Austenite Fe-Cr-Ni-Ti Alloys", Met. Trans., V. 1, (Jan. 1970), Pp. 163-170.

83. R. E. Reed-Hill, Physical Metallurgy Principles, Van Nostrand Reinhold Co., New York, (1969), P. 487.
84. M. I. Chaevskii and V. V. Popovich, "Mechanisms of Corrosion Cracking of Metals Deformed in Contact with Molten Lithium", Fiziko-Khimicheskaya Mekhanika Materialov, V. 6, No. 5, (1970), Pp. 106-108.